LAMOST OBSERVATIONS IN THE *KEPLER* FIELD. I. DATABASE OF LOW-RESOLUTION SPECTRA[*]

P. De Cat[2], J. N. Fu[1], A. B. Ren[2], X. H. Yang[2], J. R. Shi[3], A. L. Luo[3], M. Yang[3], J. L. Wang[3], H. T. Zhang[3], H. M. Shi[3], W. Zhang[3], Subo Dong[4], G. Catanzaro[5], C. J. Corbally[6], A. Frasca[5], R. O. Gray[7], J. Molenda-Żakowicz[8,9], K. Uytterhoeven[10,11], M. Briquet[12,13], H. Bruntt[14], S. Frandsen[14], L. Kiss[15], D. W. Kurtz[16], M. Marconi[17], E. Niemczura[8], R. H. Østensen[18], V. Ripepi[17], B. Smalley[19], J. Southworth[19], R. Szabó[15], J. H. Telting[20], C. Karoff[14,21], V. Silva Aguirre[14], Y. Wu[3], Y. H. Hou[22], G. Jin[23], and X. L. Zhou[24]

[1] Department of Astronomy, Beijing Normal University, 19 Avenue Xinjiekouwai, Beijing 100875, China; Peter.DeCat@oma.be
[2] Royal observatory of Belgium, Ringlaan 3, B-1180 Brussel, Belgium
[3] Key Lab for Optical Astronomy, National Astronomical Observatories, Chinese Academy of Sciences, Beijing 100012, China
[4] Kavli Institute for Astronomy and Astrophysics, Peking University, Yi He Yuan Road 5, Hai Dian District, Beijing, 100871, China
[5] INAF—Osservatorio Astrofisico di Catania, Via S. Sofia 78, I-95123 Catania, Italy
[6] Vatican Observatory Research Group, Steward Observatory, Tucson, AZ 85721-0065, USA
[7] Department of Physics and Astronomy, Appalachian State University, Boone, NC 28608, USA
[8] Astronomical Institute of the University of Wrocław, ul. Kopernika 11, 51-622 Wrocław, Poland
[9] New Mexico State University, Department of Astronomy, P.O. Box 30001, MSC 4500, Las Cruces, NM 88003, USA
[10] Instituto de Astrofísica de Canarias (IAC), E-38200 La Laguna, Tenerife, Spain
[11] Universidad de La Laguna, Dept. Astrofísica, E-38206 La Laguna, Tenerife, Spain
[12] Institut d'Astrophysique et de Géophysique, Université de Liège, Allée du 6 Août 19C, B-4000 Liège, Belgium
[13] LESIA, Observatoire de Paris, PSL Research University, CNRS, Sorbonne Universités, UPMC Univ. Paris 06, Univ. Paris Diderot, Sorbonne Paris Cité, France
[14] Stellar Astrophysics Center, Department of Physics and Astronomy, Aarhus University, Ny Munkegade 120, DK-8000 Aarhus C, Denmark
[15] Konkoly Observatory, Research Center for Astronomy and Earth Sciences, Hungarian Academy of Sciences, Konkoly Thege Miklós út 15-17. H-1121 Budapest, Hungary
[16] Jeremiah Horrocks Institute, University of Central Lancashire, Preston PR1 2HE, UK
[17] INAF—Osservatorio Astronomico di Capodimonte, via Moiariello 16, I-80131 Napoli, Italy
[18] Instituut voor Sterrenkunde, KU Leuven, Celestijnenlaan 200D, B-3001 Leuven, Belgium
[19] Astrophysics Group, Keele University, Staffordshire, ST5 5BG, UK
[20] Nordic Optical Telescope, Rambla José Ana Fernández Pérez 7, E-38711 Breña Baja, Spain
[21] Department of Geoscience, Aarhus University, Høegh-Guldbergs Gade 2, DK-8000, Aarhus C, Denmark
[22] Nanjing Institute of Astronomical Optics & Technology, National Astronomical Observatories, Chinese Academy of Sciences, Nanjing 210042, China
[23] University of Science and Technology of China, Hefei 230026, China
[24] Key Laboratory of Space Astronomy and Technology, National Astronomical Observatories, Chinese Academy of Sciences, Beijing 100012, China

ABSTRACT

The nearly continuous light curves with micromagnitude precision provided by the space mission *Kepler* are revolutionizing our view of pulsating stars. They have revealed a vast sea of low-amplitude pulsation modes that were undetectable from Earth. The long time base of *Kepler* light curves allows for the accurate determination of the frequencies and amplitudes of pulsation modes needed for in-depth asteroseismic modeling. However, for an asteroseismic study to be successful, the first estimates of stellar parameters need to be known and they cannot be derived from the *Kepler* photometry itself. The *Kepler* Input Catalog provides values for the effective temperature, surface gravity, and metallicity, but not always with sufficient accuracy. Moreover, information on the chemical composition and rotation rate is lacking. We are collecting low-resolution spectra for objects in the *Kepler* field of view with the Large Sky Area Multi-Object Fiber Spectroscopic Telescope (LAMOST, Xinglong observatory, China). All of the requested fields have now been observed at least once. In this paper, we describe those observations and provide a useful database for the whole astronomical community.

Key words: astronomical databases: miscellaneous – stars: fundamental parameters – stars: general – stars: statistics

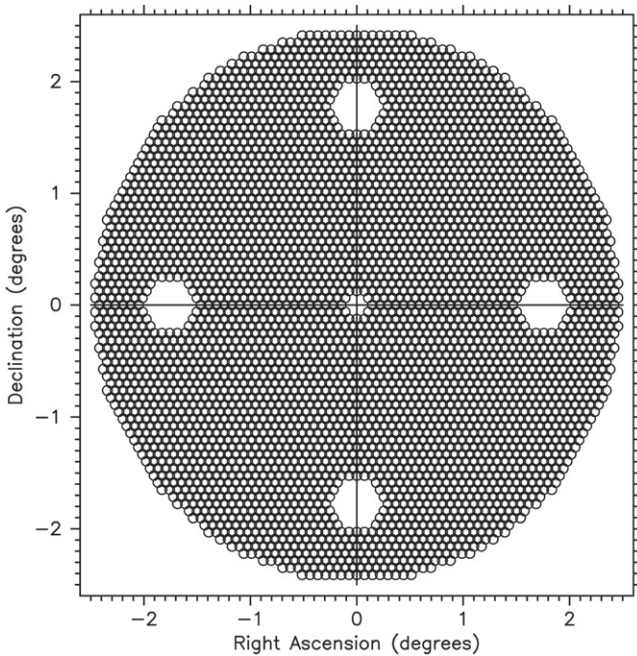*Supporting material:* machine-readable tables

1. INTRODUCTION

The space mission *Kepler* was designed to detect Earth-like planets around solar-type stars using the transit method (Koch et al. 2010). It was launched on 2009 March 7 and started to collect ultraprecise photometry within a spectral bandpass from 400 to 850 nm for a fixed field of view (FOV) of 105 square degrees in the constellations Lyra and Cygnus on 2009 May 2. On 2013 May 11, the second of four reaction wheels on the *Kepler* spacecraft failed, preventing the telescope from precisely pointing toward the same FOV. Even though ultrahigh precision photometry can no longer be collected in the original *Kepler* FOV, the *Kepler* photometry that is now available for about 200,000 stars is a pure goldmine for asteroseismic studies of all types of pulsating stars, as well as for many other science cases.

The success of asteroseismic studies has been shown to depend crucially on the availability of first estimates of basic stellar parameters, such as the effective temperature ($T_{\rm eff}$), surface gravity ($\log g$), metallicity ($[M/H]$), and projected

---

Figure 1. Configuration of the 4000 fiber positioning units covering the 5° focal plane. The fibers are homogeneously distributed on the focal plane, except for the position of the active optics wave front sensor (central hole) and four Guiding CCD cameras (off-center holes).

stellar equatorial rotation velocity ($v \sin i$; Michel 2006; Cunha et al. 2007). These parameters cannot always be directly derived from the *Kepler* data, as in the case of data with multi-color photometry or spectroscopy. Before the launch of *Kepler*, there was a large effort to derive stellar parameters from Sloan photometry for potential *Kepler* targets. These are available in the *Kepler* Input Catalog (KIC; Brown et al. 2011). Unfortunately, KIC stellar parameters are not available for all of the stars of interest and the precision of T_{eff} and log g in the KIC is generally too low for asteroseismic modeling, especially for hot and peculiar stars (Molenda-Żakowicz et al. 2010b; McNamara et al. 2012). Also, detailed information on the stellar chemical composition and rotation rate is lacking. Hence, to exploit the *Kepler* data best, additional ground-based *spectroscopic* data are required (Uytterhoeven et al. 2010a, 2010b).

LAMOST (also called the Guo Shou Jing Telescope) is a unique astronomical instrument located at the Xinglong observatory (China). It combines a large aperture (3.6–4.9 m) with a wide FOV (circular with diameters of 5°; Wang et al. 1996). The focal surface is covered with 4000 optical fibers connected to 16 multi-object optical spectrometers with 250 optical fibers each (Xing et al. 1998; Figure 1). Each spectrometer has two CCD cameras: one for the blue arm (optimized for 370–590 nm) and one for the red arm (optimized for 570–900 nm). Their spectral resolution at full slit is either 1000 or 5000 depending on the use of the low- or medium-resolution grating mode and on the camera positions. During the initial LAMOST observations, it was possibile to enhance the resolution to 2000 or 10,000 by limiting the fiber slit to a 1/2 slit width for the low or medium grating mode. However, at the time of our observations, only one set of medium-resolution gratings was available and the wavelength coverage of the medium-resolution mode is restricted to 510–540 nm in the blue and 830–890 nm in the red. This grating set was not used. Moreover, at the start of the pilot survey on 2011 October 24,

the fiber slit was permanently fixed to a ×2/3 slit width for all of the LAMOST projects, corresponding to a resolution of about 1800 for the low-resolution mode. The active optics technique is used to control the reflecting corrector (Su et al. 1998). LAMOST has a quasi-meridian transit configuration capable of tracking the motion of celestial objects for about 4 hr while they are passing the meridian. For more detailed information about LAMOST, see Cui et al. (2012) and Zhao et al. (2012).

LAMOST is an excellent instrument to perform spectroscopic follow-up for targets of the *Kepler* mission because it is capable of collecting low-resolution spectra for thousands of objects down to magnitudes of 17.8 simultaneously. In 2010, we initiated the "LAMOST-*Kepler* project" (LK-project) to observe as many objects in the *Kepler* FOV as possible from the start of the test phase of LAMOST onward. This allows for a homogeneous determination of both the stellar parameters and the spectral classification of the observed objects. Moreover, with low-resolution spectra, it is possible to estimate the radial velocity (v_{rad}) and, in the case of rapid rotation, the projected rotational velocity ($v \sin i$) of the observed objects.

This paper is the first of a series dealing with the detailed description and analysis of the spectra obtained for the LK-project in the *Kepler* FOV during the first round of observations, up to the end of the 2014 observation season. The structure of this paper is as follows. In Section 2, we explain how we compiled a prioritized target list that was used as input for the LAMOST observations. In Sections 3 and 4, we justify our choice of the central positions of the different LAMOST fields that we requested to be observed and how the selection of the fibers on the fields was done, respectively. A detailed description of the observations themselves is given in Section 5. Section 6 provides an overview of the most important steps of the reduction procedure that resulted in the database of LAMOST spectra described in Section 7. The full results will be published in the subsequent papers of this series (A. Frasca et al. 2015, in preparation; R. O. Gray et al. 2015, in preparation; A. B. Ren et al. 2015, in preparation). This paper concludes with a discussion of the importance of the acquired LAMOST spectra for the community involved in *Kepler* research in Section 8.

2. SELECTION OF THE TARGETS

We constructed a prioritized list of targets for the LK-project that was used to prepare the LAMOST observations. We made use of our knowledge of objects within the *Kepler* FOV prior to the start of our LK-project, i.e., their position (R.A. α_{2000}, decl. δ_{2000}), their brightness (the KIC magnitude Kp for most of the objects; see Section 2.2), the availability of stellar parameters in the KIC (the effective temperature T_{eff}, the surface gravity log g, and the metallicity $[M/H]$), and their scientific importance within the community involved in the *Kepler* research (see Section 2.1).

2.1. Type of Targets

The first level of prioritization was based on the type of object. The targets with a specific scientific interest are presented in Figure 2. We made a distinction from high priority to low priority among the following.

1. "Standard targets" (∼120): MK secondary standard stars. These targets were originally introduced in the beginning of the LK-project because LAMOST spectra of these objects
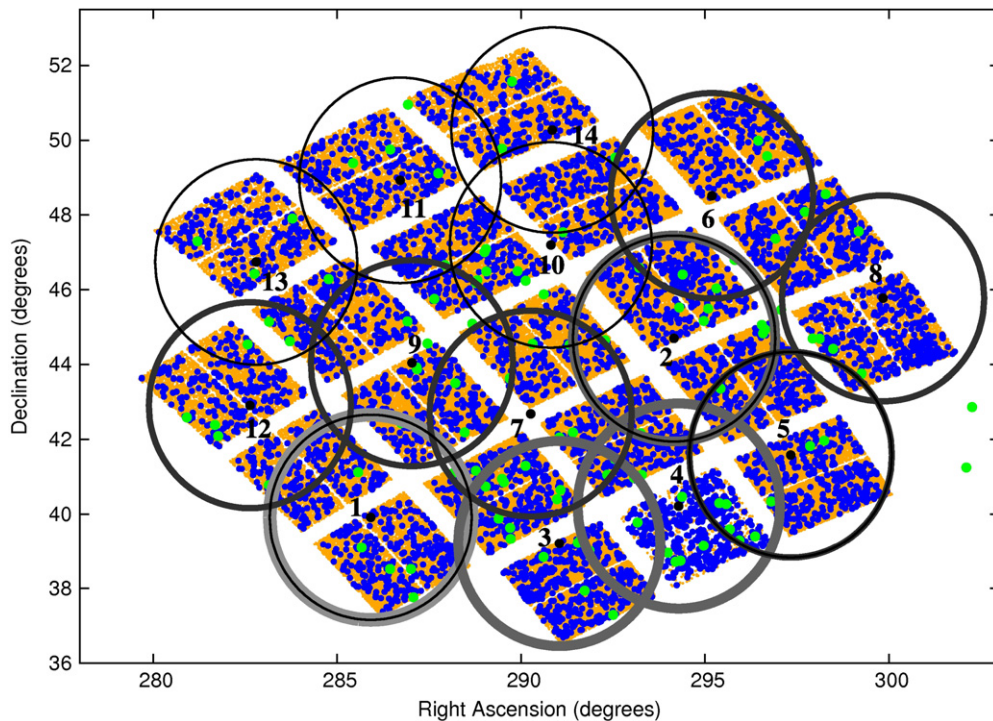
Figure 2. Targets of scientific interest in the FOV of the *Kepler* mission. The black dots refer to the centers of the 14 LK-fields that cover the *Kepler* FOV (see Table 1). The following color coding is used (from high to low scientific importance): green for standard targets, blue for KASC targets, and orange for planet targets. The scientific importance of the different types of targets within the LK-project is also reflected in the size of the symbols. The LK-fields observed in 2011–2014 are indicated by the circles drawn with a full line going from thick to thin and from gray to black, respectively.

are needed to calibrate the results of the other objects. As the project evolved, other standard stars based on earlier LAMOST observations were selected automatically.

2. "KASC targets" (∼6500): targets in the *Kepler* FOV selected by the *Kepler* Asteroseismic Science Consortium (KASC).[25] As this project was initiated by the chairs of the ground-based follow-up working groups for KASC targets, these KASC targets were considered to be of the highest scientific interest.

3. "Planet targets" (∼150,000): targets in the *Kepler* FOV selected by the *Kepler* planet search group (Batalha et al. 2010).

4. "Extra targets" (∼1,000,000): other targets in the *Kepler* FOV from the KIC (Brown et al. 2011). They have no specific scientific interest but were potential targets of the *Kepler* mission, except those that fall in the regions that are not covered by the *Kepler* CCDs (white parts on Figure 2).

Henceforth, we will refer to all these targets as *Kepler* targets. Note that there is overlap with the targets of the LAMOST project of W. Wang et al. (2015, private communication) focusing on planet host star candidates in the *Kepler* FOV. The targets of common interest received the same priority as the KASC targets from 2012 onward. It was already clear from the beginning of our project that not all of the *Kepler* targets could be observed. Initially, the aim was to observe as many of the KASC and planet targets as possible, as those targets are of a specific scientific interest. Now that the observations of the

nominal *Kepler* mission have ended, we know for which objects *Kepler* photometry is available. For the next round of observations, these 199,718 objects will be top priority.

To ensure optimal use of all of the available fibers, for each of the requested LAMOST fields (see Section 3) we provided a list of additional objects with $V < 20$ based on the USNO-B catalog (Monet et al. 2003). These "field targets" are of no particular scientific interest for our project, but since they are observable and used to fill all of the available fibers, we will obtain relevant information on them by homogeneously analyzing their spectra with the *Kepler* targets. Note that the field targets have not yet been cross-identified with the KIC when compiling the target list. This was only done afterward for all of the objects that were observed with LAMOST (see Section 7.1). Of the 38,416 objects that were originally observed as field targets, only 79 could not be reclassified as a *Kepler* target after cross-identification (see the "Unique" row in Table 1).

2.2. Brightness

Ground-based spectroscopic data are also being collected with 2 m class telescopes elsewhere (e.g., Catanzaro et al. 2010; Molenda-Żakowicz et al. 2010a, 2011, 2013; Uytterhoeven et al. 2010a; Bruntt et al. 2011, 2012; Catanzaro et al. 2011; Lehmann et al. 2011; Thygesen et al. 2012; Tkachenko et al. 2012, 2013; Karoff et al. 2013; Niemczura et al. 2015). As these observations are restricted to bright targets (generally $V < 12$), the highest priority for observations with LAMOST is given to fainter objects. However, several bright stars studied in the aforementioned works were also targeted for comparison purposes.

The exposure times for LAMOST observations can only be optimized if the brightness range of the observed targets is not

---

[25] Relevant information on KASC can be found on the *Kepler* Asteroseismic Science Operations Center (KASOC) web page http://kasoc.phys.au.dk/, maintained by Rasmus Handberg from the University of Birmingham in the United Kingdom.

Table 1
Statistical Overview of the Observations Obtained up to the End of the 2014 Observation Season for the *Kepler* FOV for the LK-project

LK-field	R.A. (2000)	decl. (2000)	Cluster	Date	#	Spectra	S	K	P	E	F	KO
LK01	19:03:39.258	+39:54:39.24	⋯	110530	1	1435	1	131	444	859	⋯	607
				110608	2	1108	4	137	336	629	2	525
				140602	2	4944	2	237	2201	2500	4	2586
LK02	19:36:37.977	+44:41:41.77	NGC6811	120604	1	582	18	131	157	273	3	355
				140913	2	6858	5	483	3504	2861	5	4171
LK03	19:24:09.919	+39:12:42.00	NGC6791	120615	3	9655	18	591	4825	4215	6	5833
LK04	19:37:08.862	+40:12:49.63	NGC6819	120617	3	9666	18	574	3785	5281	8	5282
LK05	19:49:18.139	+41:34:56.85	⋯	131005	2	6374	4	474	2704	3191	1	3487
				140522	1	2422	4	278	1048	1092	⋯	1431
LK06	19:40:45.383	+48:30:45.10	⋯	130522	1	2488	4	366	1383	735	⋯	1770
				130914	1	3037	3	237	1778	1015	4	2046
LK07	19:21:02.816	+42:41:13.07	⋯	130519	1	3025	12	416	1820	777	⋯	2303
				130523	1	2304	4	152	1590	558	⋯	1793
				130926	1	3165	8	275	1995	886	1	2357
LK08	19:59:20.425	+45:46:21.15	NGC6866	130925	2	5928	2	387	1957	3576	6	2386
				131002	1	2795	⋯	20	19	2751	5	56
				131017	1	2769	⋯	41	906	1820	2	990
				131025	1	2970	⋯	50	1024	1896	⋯	1119
LK09	19:08:08.340	+44:02:10.88	⋯	131004	1	3141	4	266	1748	1122	1	2106
LK10	19:23:14.829	+47:11:44.80	⋯	140520	2	3781	4	222	2401	1154	⋯	2683
LK11	19:06:51.499	+48:55:31.77	⋯	140918	1	3070	4	340	1572	1149	5	1940
LK12	18:50:31.041	+42:54:43.72	⋯	131007	1	2922	5	229	1329	1354	5	1590
LK13	18:51:11.993	+46:44:17.52	⋯	140502	1	2501	2	199	1102	1196	2	1345
				140529	2	4693	1	232	2091	2358	11	2434
LK14	19:23:23.787	+50:16:16.64	⋯	140917	1	3167	⋯	187	1455	1521	4	1685
				140927	1	3160	1	107	1424	1625	3	1585
				140929	1	3126	1	87	1291	1740	7	1441
Total						101,086	129	6849	45,889	48,134	85	55,906
Unique						80,447	93	4712	34,904	40,659	79	42,209
1×						63,333	65	3142	25,919	34,133	74	31,147
2×						14,186	20	1129	7286	5747	4	8859
3×						2483	8	355	1457	662	1	1870
4×						332	⋯	54	199	79	⋯	258
+5×						113	⋯	32	43	38	⋯	75

Note. The top lines give the specifications of the LK-fields that have been observed. For each LK-field, we give the right ascension (R.A. (2000)) and declination (decl. (2000)) of the central bright star, the name of the open cluster that it contains (Cluster, if applicable), the date of observation (YYMMDD; Date), the number of plates that were used to observe the LK-field (#), the total number of spectra that have been reduced successfully (Spectra), and the number of spectra for *Kepler* targets—subdivided into standard (S), KASC (K), planet (P), extra (E), targets—field targets (F), and objects that were observed by the *Kepler* mission (KO). The bottom lines give the summary of the observations of all of the LK-fields together. For each category of targets, we give the total number of spectra that have been reduced successfully (Total), the number of different objects that it contains (Unique) and the number of targets that have been observed one (1×), two (2×), three (3×), four (4×), and at least five (+5×) times.

larger than 5 mag. For the initial observations (2011 May 31, June 8, and 2012 June 4), we therefore made a distinction between three different brightness intervals from high to low priority: middle targets ($10.5 < Kp \leqslant 15.5$), bright targets ($Kp \leqslant 10.5$), and faint targets ($Kp > 15.5$). For the group of middle targets, those without KIC stellar parameters are considered as the most important ones within each type of target (standard, KASC, planet, and extra). They were prioritized according to brightness from bright to faint. Those for which KIC stellar parameters are already available were prioritized from high to low $T_{\rm eff}$ because the determination of the KIC $T_{\rm eff}$ for hot stars suffered from the lack of an ultraviolet filter in the Sloan photometry. The objects in the other brightness groups were prioritized according to brightness regardless of the availability of KIC parameters. The bright targets were prioritized from faint to bright to minimize saturation effects (too much flux) while the faint targets were prioritized from bright to faint to minimize the occurrence of underexposed objects (not enough flux). For the observations obtained after

2012 June 4, a distinction was made only between brighter ($9.0 < Kp \leqslant 14.0$) and fainter ($Kp > 14.0$) targets. The brighter and fainter targets were prioritized in the same way as the middle and faint targets from the initial observations, respectively.

3. SELECTION OF THE LAMOST FIELDS

We made use of a simplified version of the bright central star tiling method to cover the *Kepler* FOV (Cui et al. 2012). This method requires a star brighter than $V = 8$ in the center of the LAMOST FOV (for the active optics wave front sensor; central hole on Figure 1) and four fainter stars with magnitude $V < 17$ (for the guiding of the CCD cameras; off-center holes on Figure 1). We therefore started by selecting 14 circular regions with a diameter of 5°, which is the minimum to (almost) fully cover the *Kepler* FOV. We refer to them as LK-fields.

In a second step, we searched for the optimized central coordinates (α_m, δ_m) for the LK-fields that maximize the total

number of observable KASC targets. This was done by adding/ subtracting 0, 1, or 2 steps of 5 arcsec each to/from the central coordinates of the original LK-fields. Finally, we searched for the bright stars with $V < 8$ that are the closest to the resulting α_m and δ_m values. These bright stars are indicated by the numbers in Figure 2. The specifications of the corresponding final LK-fields are given in Table 1. The LK-fields are given in the suggested observation order, which was chosen to maximize the number of observable KASC targets. Note that four of the LK-fields contain an open cluster (NGC 6791, NGC 6811, NGC 6819, and NGC 6866). Since the members of open clusters have more constraints on the input parameters that can be used for asteroseismic modeling (such as a common age and metallicity), the priority of the LK-fields containing an open cluster has been increased according to the asteroseismic potential of the open cluster. Unfortunately, because of the high density of the objects in these regions, it is impossible to observe all of the targets of scientific interest in the LK-fields containing an open cluster.

4. SELECTION OF THE FIBERS

LAMOST is equipped with 4000 optical fibers. All of the fibers have a diameter of 320 μm corresponding to 3.3 arcsec on the sky (Cui et al. 2012). A new system for the positioning of the fibers, called the "distributive parallel-controllable fiber positioning system," has been developed (Xing et al. 1998). The focal plane of the telescope with a diameter of 1.75 m (5°) is covered by 4000 fiber positioning units whose configuration is shown in Figure 1. Each unit covers a circular area with a diameter of 33 mm (340 arcsec) on the focal surface and contains one fiber that can reach all of the places within this area (Cui et al. 2012). There is some overlap between the areas to ensure that there is no blind space on the focal surface. The 4000 fibers can all move separately and accurate positioning of the fibers only takes about 10 minutes. The total preparation time for an exposure, including the focus procedure, is about half an hour.

The code "Survey Strategy System" was used to prepare the observation plans of the LK-project to optimize the effective use of the fibers (Cui et al. 2012). The prioritized list of targets (see Section 2) and the equatorial coordinates of the selected bright central stars of the LK-fields (see Section 3) were used as input for the distribution of the fibers. During the allocation of the fibers, two basic rules apply: the number of observed objects should be maximized and objects that can be observed by more than one unit should be allocated to the unit that is the nearest to them to reduce the probability of mechanical collisions during the observations. For each spectrograph, at least 5 fibers should be allocated to standard targets whose flux is known to allow a flux calibration of the LAMOST spectra, and 20 fibers should be pointing toward an object-free region to allow an accurate correction for the contribution from the sky. The displacement of a fiber from an object is determined by measuring the flux changes of objects passing through the fibers when the telescope points to different positions around the center of a sky field. The displacements of the 4000 fibers are used to build a coordinate relation between the focal surface and the celestial coordinates. For more details about these procedures, we refer interested readers to Cui et al. (2012).

5. OBSERVATIONS

As only one LK-field was observed per night, covered by, at maximum, three different plates (=unique configurations of the fibers), a strict minimum of 14 observation nights was required to observe all of the requested LK-fields of the LK-project. This was due to both the limitations of LAMOST and the visibility of the *Kepler* FOV. The observation of a LK-field can last at most 4 hr while the celestial objects are passing the meridian. However, as the observable period of the *Kepler* FOV coincides for a large part with the Monsoon (the Xinglong observatory is closed from mid-June to mid-September), the observations can only be done from late-May to mid-June (with a maximal observation window of 2 hr before meridian passage) and from mid-September to late-October (with a maximal observation window of 2 hr after meridian passage). About half an hour is needed to focus the system and CCD readout takes 8 minutes. In general, 30 minutes (3×600 s) are required to observe a "V-plate" (containing objects with a magnitude range of $9 < r \leqslant 14$) and 75 minutes ($3 \times 1\,500$ s) for a "B-plate" (containing objects with a magnitude range of $14 < r \leqslant 16.3$; see Table 2 from 2013 onward). For these reasons, four observation seasons of the *Kepler* FOV were needed to finish the first round of observations for the LK-project.

A total of 38 plates were observed on 27 different observation nights. The earliest observations (in 2011 May and June) were performed during the test phase of LAMOST. The 2012 observations were obtained during the pilot survey of LAMOST (from 2011 October 24 until 2012 June 24). The more recent observations date from the general survey phase of LAMOST. The LK-fields that were observed in the period 2011–2014 are indicated in Figure 2 by the circles drawn with a full line going from thick to thin and from gray to black, respectively. In Table 2, we provide an overview of the specifications of the observed plates for the LK-project so far. In 2011, the resolution of the observations was either $R = 1000$ (slit position "×1") or 2000 (slit position "×1/2"), while the resolution from 2012 onward was fixed to $R \sim 1800$ (slit position "×2/3"). The observation of a LAMOST plate can last at maximum 4 hr as celestial objects can be observed from about 2 hr before to 2 hr after the passage at meridian. The observation times of the sub-exposures of the plates were adjusted according to the brightness of the targets and to the weather conditions. From 2013 onward, the observed plates are called a "V-plate," "B-plate," "M-plate," and "F-plate" for targets with $9 < r \leqslant 14$, $14 < r \leqslant 16.3$, $16.3 < r \leqslant 17.8$, and $17.8 < r \leqslant 18.5$, respectively. Under normal circumstances, their observation times are 3×10 minutes, 3×25 minutes, 3×30 minutes, and 3×30 minutes, respectively (ΔT_{sub} in Table 2).

Before the Monsoon break of 2011, there were system errors between the astronomical coordinate system and the physical coordinates on the focal plane, leading to many low-quality spectra. Thanks to a calibration of the system coordinates using the stellar objects on the sky, the whole system error could be reduced to less than 0.5 arcsec. Currently, the positioning errors can be compensated for in real time, ensuring a positioning accuracy of less than 40 μm, i.e., about 0.4 arcsec (Cui et al. 2012).

Before the pilot survey, there were occasional failures of the dewar system because of an exhaustion of the liquid nitrogen. Images taken under these circumstances are dominated by

Table 2
Overview of the Specifications of the Observed Plates for the LK-project from 2011 to 2014

Plate	LK-field	$\Delta T_{\rm tot}$ (s)	$\Delta T_{\rm sub}$ (s)	Slit	Seeing (arcsec)	Transparency	Observer
110530_1	LK01	2400	2×1200	$\times 1$	~2.75	mostly clear	Wei Zhang
110608_1	LK01	900	$1 \times 600 + 1 \times 300$	$\times 1/2$	~3.60	clear	Jianrong Shi
110608_2	LK01	1200	2×600	$\times 1/2$	~3.60	clear	Jianrong Shi
120604_1	LK02	600	2×300	$\times 2/3$	~3.10	poor	Huoming Shi
120615_1	LK03	1600	$2 \times 600 + 1 \times 400$	$\times 2/3$	~3.75	mostly cloudy	Jianrong Shi
120615_2	LK03	1300	$2 \times 400 + 1 \times 500$	$\times 2/3$	~3.25	mostly cloudy	Jianrong Shi
120615_3	LK03	2400	2×1200	$\times 2/3$	~3.75	mostly cloudy	Jianrong Shi
120617_1	LK04	900	$1 \times 400 + 1 \times 500$	$\times 2/3$	~4.45	cloudy	Jianrong Shi
120617_2	LK04	900	$1 \times 400 + 1 \times 500$	$\times 2/3$	~3.90	cloudy	Jianrong Shi
120617_3	LK04	1200	1×1200	$\times 2/3$	~4.00	cloudy	Jianrong Shi
130519_1	LK07	3000	5×600	$\times 2/3$	~3.50	clear	Jianling Wang
130522_1	LK06	2100	3×700	$\times 2/3$	~3.25	cloudy	Jianling Wang
130523_1	LK07	3600	4×900	$\times 2/3$	~3.80	cloudy	Jianling Wang
130914_1	LK06	1800	3×600	$\times 2/3$	~3.10	clear	Jianling Wang
130925_1	LK08	1800	3×600	$\times 2/3$	~3.90	clear	Ming Yang
130925_2	LK08	1800	3×600	$\times 2/3$	~4.10	clear	Ming Yang
130926_1	LK07	1800	3×600	$\times 2/3$	~4.40	clear	Ming Yang
131002_1	LK08	4930	$2 \times 1800 + 1 \times 1330$	$\times 2/3$	~3.90	clear	Wei Zhang
131004_1	LK09	1200	2×600	$\times 2/3$	~3.60	cloudy	Jianrong Shi
131005_1	LK05	1800	3×600	$\times 2/3$	~3.30	cloudy	Jianrong Shi
131005_2	LK05	1800	3×600	$\times 2/3$	~3.50	cloudy	Jianrong Shi
131007_1	LK12	1800	3×600	$\times 2/3$	~3.10	clear	Jianrong Shi
131017_1	LK08	1800	3×600	$\times 2/3$	~3.30	cloudy	Jianling Wang
131025_1	LK08	1800	3×600	$\times 2/3$	~3.00	clear	Ming Yang
140502_1	LK13	2400	4×600	$\times 2/3$	~3.50	mostly clear	Jianling Wang
140520_1	LK10	1500	1×1500	$\times 2/3$	~3.20	mostly clear	Jianrong Shi
140520_2	LK10	2400	4×600	$\times 2/3$	~3.10	mostly clear	Jianrong Shi
140522_1	LK05	1200	2×600	$\times 2/3$	~3.40	clear	Jianrong Shi
140529_1	LK13	1800	3×600	$\times 2/3$	~3.70	clear	Wei Zhang
140529_2	LK13	1800	3×600	$\times 2/3$	~3.40	clear	Wei Zhang
140602_1	LK01	1800	3×600	$\times 2/3$	~3.10	clear	Ming Yang
140602_2	LK01	1800	3×600	$\times 2/3$	~3.10	clear	Ming Yang
140913_1	LK02	1800	3×600	$\times 2/3$	~3.00	mostly clear	Ming Yang
140913_2	LK02	1800	3×600	$\times 2/3$	~3.20	mostly clear	Ming Yang
140917_1	LK14	1800	3×600	$\times 2/3$	~3.20	clear	Ming Yang
140918_1	LK11	1800	3×600	$\times 2/3$	~3.20	clear	Ming Yang
140927_1	LK14	1800	3×600	$\times 2/3$	~3.80	partly cloudy	Jianrong Shi
140929_1	LK14	1800	3×600	$\times 2/3$	~4.30	clear	Jianrong Shi

Note. For each plate, we give the date with the sequence number of the plate (YYMMDD_N; Plate), the reference of the LK-field that was observed (LK-field, see Table 1), the total integration time ($\Delta T_{\rm tot}$), and the integration times of the sub-exposures ($\Delta T_{\rm sub}$) in seconds, the slit width (Slit), the estimated value of the seeing (Seeing), an indication of the transparency of the sky during the observations (Transparency), and the name of the observer (Observer).

thermal noise due to the rising temperature of the CCD chip, making data obtained under these conditions useless. Moreover, there are approximately 110 known bad fibers because either they were broken or their fiber positioners did not work properly. Those fibers were excluded from the reduction pipeline.

6. REDUCTIONS

The main products of LAMOST are wavelength and flux-calibrated spectra which are provided to astronomers. They are processed by a data reduction pipeline and an analysis pipeline. In the following subsections, we provide short descriptions of the most important reduction steps which are relevant to our project. The analysis pipeline includes the classification and identification of the spectra and the measurement of the spectral parameters of the observed objects. For more details about

pipeline procedures, we refer interested readers to Luo et al. (2012) and Luo et al. (2015).

6.1. Pipeline

The data reduction pipeline consists of 2D and 1D procedures. The LAMOST 2D procedure is used to reduce separately the data from each of the 32 CCD chips (2 for each spectrograph) and of each exposure. Apart from the science frames themselves, the 2D pipeline also makes use of the series of bias, dark, arc lamp, and sky flat-field frames that are taken at the beginning of each observation night. The reduction procedure consists of several steps. The bias and dark frames are combined into a master bias and a master dark frame each night and they are both subtracted from each raw image. From the general survey onward, the dark subtraction is not necessary any longer because the problem with an inside

CCD light source that affected the images has been eliminated. For each CCD chip, 250 1D spectra are extracted from the raw data by using the row positions derived from the flat-field frames. For each region of the sky covered by one spectrograph, a super sky based on the sky measurements of at least 20 fibers is created to model and subtract the contribution of the background. This step is important because the telluric continuum and lines, if not properly subtracted, affect the following analysis, especially for the faintest targets. The centroids of the lines of the arc lamp spectra are measured and a Legendre polynomial is fit to their wavelengths as a function of the pixels. A vacuum wavelength scale is applied for the wavelength calibration and the resulting wavelength calibrations are accurate to $10 \mathrm{\,km\,s^{-1}}$ (or better). Also, the helio-centric corrections are applied. The difference in the efficiency of the different fibers is corrected for by dividing with a super flat that is constructed by combining the extracted, wavelength-calibrated, and re-scaled sky flat-field frames. The telluric absorption lines are removed in four wavelength regions (685–696 nm; 715–735 nm; 756–772 nm; 810–824 nm). The spectra are flux calibrated by matching the instrumental fluxes in the LAMOST spectra of the observed standard targets with tabulated values in energetic units. The spectra from the red and blue arms of each spectrograph are combined by stacking the points with corresponding wavelengths using a B-spline function with inverse variance weighting. Outliers due to cosmic rays are rejected and masked and the errors in flux are estimated. The combined spectra are re-sampled to constant velocity pixels with a pixel scale of $69 \mathrm{\,km\,s^{-1}}$, which corresponds to a wavelength difference of $\Delta \log(\lambda) = 0.0001$.

In the LAMOST 1D procedure, the reduced spectra from the LAMOST 2D procedure are used to estimate the spectral class and v_{rad} of the observed targets. These characteristics are based on template matching since, for low signal-to-noise ratio (S/N) spectra, the fitting and measurement of spectral lines is not precise. The v_{rad} determination is performed with a generalized version of the cross-correlation technique. The analysis code estimates the spectral type (SpT) of the observed targets by making χ^2 fits in wavelength space of their LAMOST spectra to templates that were constructed from a set of Sloan Digital Sky Survey (SDSS) spectra. The results are checked through a comparison of the lines of the observed spectrum with those from the best-fit template. If they are very different, then it is decided by a visual check whether or not the classification is correct. The 1D pipeline only gives results for spectra with a $\mathrm{S/N} > 5$. After a comparison of the results with the SpTs and radial velocities of the observed SDSS stars, it turns out that 96% of the spectra with $\mathrm{S/N} > 10$ in the r band are classified correctly and an accuracy of $13 \mathrm{\,km\,s^{-1}}$ can be reached for v_{rad}.

6.2. Combination of the Sub-exposures

For LAMOST, the observation of each plate generally consists of more than one sub-exposure (see Table 2). This observation strategy is preferred because it makes it possible both to subtract the cosmic rays from the CCDs and to improve the S/N by combining the flux of the sequential sub-exposures. The wavelength and flux calibration are performed for each sub-exposure individually to overcome the unstable effects of the instrument (such as tracking and pointing) and the temporal variations of the weather. In the first step, these sub-spectra are scaled to the same level before putting them together. As the wavelength samples of the sub-spectra are not exactly the same, the combined spectrum is over-sampled. In a second step, this combined spectrum is smoothed and re-sampled by a spline function. Note that if the same field was observed on different nights, the spectra are not summed because the calibration is different for each night and the observed object might be a variable.

7. DATABASE

A total of 38 plates have been observed so far for the LK-project. Unfortunately, due to the pointing problems and/or the malfunctioning of some of the spectrographs and/or fibers (Section 5), the raw spectra for a fraction of the observed objects could not be reduced by the reduction pipeline for some of the nights, especially during the test phase and the pilot survey in 2011 and 2012 (Section 6). This is reflected both in the amount of missing spectrograph numbers in Table 3 and in the evolution of the success rate of the LAMOST reduction pipeline for the LK-project, as shown by the full, light gray line in Figure 8. In the LK-project, only LAMOST observations for which both the 2D and 1D reduction procedures could be applied successfully are analyzed. We did not include in the database those spectra for which the 1D reduction procedure classified the object as either "Unused" (fiber is not used), "Unassigned" (fiber is not assigned), "Dead" (fiber is not working), or "Sky" (fiber is used to measure the flux of the sky). This results in 101,086 entries in the database for a total of 80,447 different targets. In Table 1, we provide the distribution of these targets for each of the observed LK-fields. In Table 3, we give an overview of the name structure of the files containing the LAMOST spectra and of the spectrograph identification numbers for which LAMOST data are available for the different plates of different nights.

We have constructed a database of these 101,086 LAMOST spectra available from the LK-project so far (Tables 4 and 5). The LAMOST 1D fits files of the LAMOST spectra, including those for the LK-project, that have already been released to the public can be downloaded from LAMOST's official website.[26] The LAMOST 1D fits files of the unreleased spectra that were made available to us by the LAMOST team can be obtained upon request[27] after becoming an external collaborator of the LK-project.[28] In column 8 of Table 4, we give the most recent version of the pipelines for which the results are available. The first two numbers refer to the reduction pipeline and the last number to the analysis pipeline. Note that v2.7.5 refers to the most recent versions that are available at this moment. The spectra emerging from an older version of the reduction pipeline can be used at one's own risk. The structure of the names of the LAMOST 1D fits files is as follows: spec-MMMMM-YYYY_spXX-FFF.fit where MMMMM gives the LAMOST modified Julian day number (LJDN; see note of Table 3 for the definition), YYYY denotes the plan identification number, and XX and FFF are the spectrograph and fiber identification number, respectively. The LJDN and plan identification number (planID) of the observed plates are given in Table 3.

[26] The LAMOST 1D fits files of the released spectra of the LK-project can be downloaded from LAMOST's official website: http://www.lamost.org/

[27] The LAMOST 1D fits files of the unreleased spectra of the LK-project can be requested by e-mail to Peter De Cat: Peter.DeCat@oma.be

[28] Requests to become an external collaborator of the LK-project should be sent by e-mail to Jianning Fu: jnfu@bnu.edu.cn

Table 3
Overview of the LAMOST 1D Fits Files Available from Observations for the LK-project from 2011 to 2014

Plate	LJDN (⋆)	planID	Version	Spectrographs															
110530_1	55712	IF10M	v2.6.5	01	02	03	04	05	06							13			
110608_1	55721	IF10B	v2.6.5	01		03	04	05	06	07								15	
110608_2	55721	IF10M	v2.4.4						06				10			13		15	
120604_1	56083	IF04_B56083	v2.7.5	01		03				07	08	09		11	12	13	14	15	16
120615_1	56094	kepler05B56094	v2.7.5	01	02	03	04	05	06	07		09	10	11	12	13	14	15	16
120615_2	56094	kepler05B56094_2	v2.7.5	01	02	03	04	05	06	07		09	10	11	12	13	14	15	16
120615_3	56094	kepler05F56094	v2.7.5	01	02	03		05	06	07		09	10	11	12	13	14	15	16
120617_1	56096	kepler08B56096_1	v2.7.5	01	02	03		05	06	07	08	09		11	12	13	14	15	16
120617_2	56096	kepler08B56096_2	v2.7.5	01	02	03		05	06	07	08	09	10	11	12	13	14	15	16
120617_3	56096	kepler08F56096	v2.7.5	01	02	03		05	06	07	08	09	10		12	13	14	15	16
130519_1	56432	KP192102N424113V01	v2.7.5	01	02	03	04	05	06	07	08	09	10	11	12	13	14	15	16
130522_1	56435	KP194045N483045V01	v2.7.5	01		03	04	05	06	07	08	09		11	12	13	14	15	16
130523_1	56436	kepler02_1	v2.7.5	01	02	03		05	06	07	08	09	10	11	12	13	14	15	16
130914_1	56550	KP194045N483045V02	v2.7.5		02	03	04	05		07	08	09	10	11	12	13	14	15	16
130925_1	56561	KP195920N454621V01	v2.7.5	01	02	03	04	05	06	07	08	09	10	11	12	13	14	15	
130925_2	56561	KP195920N454621V02	v2.7.5	01	02	03	04	05	06	07	08	09	10	11	12	13	14	15	
130926_1	56562	KP192102N424113V02	v2.7.5	01	02	03	04	05	06	07	08	09	10	11	12	13		15	16
131002_1	56568	KP195920N454621M01	v2.7.5	01	02	03	04	05		07	08	09	10	11	12		14	15	16
131004_1	56570	KP190808N440210V01	v2.7.5	01	02	03	04	05	06	07	08	09	10	11	12	13	14	15	16
131005_1	56571	KP194918N413456V01	v2.7.5	01	02	03	04	05	06	07	08	09	10	11	12	13	14	15	16
131005_2	56571	KP194918N413456V02	v2.7.5	01	02	03	04	05	06	07	08	09	10	11	12	13	14	15	16
131007_1	56573	KP185031N425443V01	v2.7.5	01	02	03	04	05		07	08	09	10	11	12	13	14	15	16
131017_1	56583	KP195920N454621V03	v2.7.5		02	03	04	05		07	08	09	10	11	12	13	14	15	16
131025_1	56591	KP195920N454621V3	v2.7.5	01	02	03	04	05		07	08	09	10	11	12	13	14	15	16
140502_1	56780	KP185111N464417V01	v2.7.5	01	02	03	04	05	06	07	08	09	10		12		14	15	16
140520_1	56798	KP192314N471144B01	v2.7.5	01		03	04	05	06				10	11	12			15	
140520_2	56798	KP192314N471144V01	v2.7.5	01	02	03	04	05	06	07	08	09	10	11	12	13	14	15	16
140522_1	56800	KP194918N413456V	v2.7.5	01	02	03	04	05	06	07	08	09	10	11		13	14	15	16
140529_1	56807	KP185111N464417V02	v2.7.5	01	02	03	04	05	06	07	08	09	10		12	13	14	15	
140529_2	56807	KP185111N464417V03	v2.7.5	01	02	03	04	05	06	07	08	09	10	11	12	13	14	15	
140602_1	56811	KP190339N395439V01	v2.7.5	01	02	03	04	05	06	07		09			12	13	14	15	16
140602_2	56811	KP190339N395439V02	v2.7.5	01	02	03	04	05	06		08	09	10	11	12	13	14	15	16
140913_1	56914	KP193637N444141V01	v2.7.5	01	02	03	04	05	06	07	08	09	10	11	12	13	14	15	16
140913_2	56914	KP193637N444141V02	v2.7.5	01	02	03	04	05	06	07	08	09	10	11	12	13	14	15	16
140917_1	56918	KP192323N501616V	v2.7.5	01	02	03	04	05	06	07		09	10	11	12	13	14	15	16
140918_1	56919	KP190651N485531V01	v2.7.5	01	02	03	04	05	06	07		09	10	11	12	13	14	15	16
140927_1	56928	KP192323N501616V02	v2.7.5	01	02	03	04		06	07	08	09	10	11	12	13	14	15	16
140929_1	56930	KP192323N501616V03	v2.7.5	01	02	03	04	05	06	07	08	09	10	11	12	13	14		16

Note. For each plate, we give the date with the sequence number of the plate (YYMMDD_N; Plate), the LAMOST modified Julian day number (LJDN; see note (⋆) below for the definition) and the plan identification number (planID) as used in the name structure of the LAMOST 1D fits files, the latest available version of the reduction pipeline (first two numbers) and analysis pipeline (last number) for which the results are available (Version), and spectrograph identification numbers for which data is available in the remaining columns (Spectrographs).
(⋆) The LAMOST modified Julian day number (LJDN) is the integer part of the LAMOST modified Julian date (LJD), which is defined as the modified Julian date (=JD—2400000.5) after adding 20 hr (5/6). This places the start of the LJD timescale at 1858 November 16 at noon in local Beijing time. Hence, all of the LAMOST data obtained during one observation night will have the same LJDN.

7.1. Cross-identification

For all of the available LAMOST 1D fits files, we cross-checked whether or not the observed objects could be identified with a *Kepler* object from KIC. The R.A. and decl. of the positions of the fibers as recorded in the headers in the LAMOST 1D fits files (see columns 9 and 10 in Table 4) were used as input for the KIC search tool.[29] These coordinates generally correspond to the equatorial coordinates of the objects as given in the target list. For a fraction of those objects brighter than magnitude 11, an offset is added to the pointing of the fibers to avoid saturation. The term "offset" refers here to the difference between the equatorial coordinates of the position of the fibers and the coordinates of the observed object as given in the target list. The objects that were flagged as having a large offset are marked with "N1" in column 14 of Table 4.

We initially searched for objects within the default search radius of 0.02 arcmin of these coordinates. If no *Kepler* object was found in this region, then we enlarged the search region to a maximum radius of 0.16 arcmin (=10 arcsec). Objects for which the cross-identification was only found with such a larger search radius are marked with "N2" or "N3" in column 14 of Table 4 and column 16 of Table 5. The few observations for which another KIC object better matches the equatorial coordinates of the fiber than the *Kepler* target mentioned in the headers of the LAMOST 1D fits files (column 3 of Table 4) are marked with "N4" to "N15" in column 14 of

---

[29] The *Kepler* Input Catalog can be consulted with the KIC search tool: http://archive.stsci.edu/kepler/kic10/search.php

Table 4
Database of the LAMOST Spectra Obtained for the LK-project: Information Extracted from the Headers of the LAMOST 1D Fits files

(1) File Name	(2) Target	(3) ID	(4) yyyy-mm-ddThh:mm:ss.ss	(5) Type	(6) KO	(7) Slit	(8) Version
(9) R.A.deg (°)	(10) decl.deg (°)	(11) MAGtype	(12) MAG (mag)	(13) S/N_r	(14) Notes		
spec-55712-IF10M_sp01-001	KIC02140382	ZHT17_Std_0000110	2011-05-30T19:01:19.98	E	N	x1	v2.6.5
285.914888	37.548585	SSA_BR2I	14.95	49.81			
spec-55712-IF10M_sp01-002	KIC01995622	extra00011944	2011-05-30T19:01:19.98	P	Y	x1	v2.6.5
286.184208	37.482444	Kp	13.52	112.71			
spec-55712-IF10M_sp01-003	KIC01994759	ZHT17_Std_0000095	2011-05-30T19:01:19.98	E	N	x1	v2.6.5
285.926985	37.494571	SSA_BR2I	16.73	9.25			
spec-55712-IF10M_sp01-004	KIC02141025	extra00014786	2011-05-30T19:01:19.98	E	N	x1	v2.6.5
286.134417	37.560833	Kp	14.83	41.10			
spec-55712-IF10M_sp01-005	KIC01995904	extra00012008	2011-05-30T19:01:19.98	E	N	x1	v2.6.5
286.261583	37.482583	Kp	14.94	47.37			
spec-55712-IF10M_sp01-006	KIC02283124	extra00018771	2011-05-30T19:01:19.98	P	Y	x1	v2.6.5
286.034917	37.664778	Kp	12.62	202.07			
spec-55712-IF10M_sp01-008	KIC02283334	extra00018819	2011-05-30T19:01:19.98	P	Y	x1	v2.6.5
286.104708	37.604194	Kp	15.37	33.25			
spec-55712-IF10M_sp01-009	KIC02282652	extra00018639	2011-05-30T19:01:19.98	P	Y	x1	v2.6.5
285.862583	37.682472	Kp	15.01	51.25			
spec-55712-IF10M_sp01-010	KIC02283496	extra00018853	2011-05-30T19:01:19.98	P	Y	x1	v2.6.5
286.155583	37.667000	Kp	15.29	42.23			
spec-55712-IF10M_sp01-011	KIC02422998	kplr002422998	2011-05-30T19:01:19.98	K	Y	x1	v2.6.5
286.192417	37.740083	Kp	10.63	531.39			

Note. Only the first 10 entries are shown. For a description of the columns, we refer to the text (see Section 7.2). For clarity, columns (9)–(14) are given on a second line for each entry.

(This table is available in its entirety in machine-readable form.)

Table 4 and column 16 of Table 5. All of the marked cross-identifications should be treated with caution. In the case where an object could be cross-identified with a KIC object, we adopted the KIC number as the final identification of the object and retrieved the KIC values of the stellar parameters ($T_{\rm eff}$, log g, and $[M/H]$), the reddening ($E(B-V)$), the contamination factors, and proper motions and listed them in the database if available (see Table 5).

An overview of the "angular separation" between the equatorial coordinates of these cross-identified objects and the equatorial coordinates of the position of their fiber (column 5 of Table 5) as a function of their *Kepler* magnitude Kp (column 7 of Table 5) is given in Figure 3. The higher the angular separation, the more doubtful is the cross-identification. The horizontal dashed line indicates the standard search radius of 0.02 arcmin around the equatorial coordinates of the position of the fibers. The top panel shows the observed objects that were listed as KIC objects in the target list. It clearly shows that the angular separations of these objects are minimal, except for a fraction of the targets with magnitude Kp > 11. The amount of offset that has been added to the pointings of the fibers is related to the brightness of these objects. The bottom panel shows those objects that were originally observed as a field target but which were cross-identified with a KIC object. For these targets, the "offset" and "angular separation" are not expected to be identical as their coordinates given in the target list originate from the USNO-B Catalog (Monet et al. 2003) and not from KIC (Brown et al. 2011). Indeed, for these objects, large angular separations are found for objects of all magnitudes and no clear relation is found between the angular separation and the brightness of the observed objects. We recall

that the cross-identifications of targets with a large angular separation should be treated with caution.

7.2. Description

For all of the LAMOST spectra in the database, Table 4 lists information contained in or extracted from the headers of their 1D fits file. This table contains the following columns.

1. Column 1: the file name of the LAMOST 1D fits file (File Name).
2. Column 2: the final identification of the target after cross-identification with the KIC catalog (Target).
3. Column 3: the identification of the target as given in headers of the LAMOST 1D fits file (ID).
4. Column 4: the date and time (Obs) of mid-exposure (yyyy-mm-ddThh:mm:ss.ss).
5. Column 5: the type of target (Type). The standard targets are indicated with "S," KASC targets with "K," planet targets with "P," extra targets with "E," and field targets with "F".
6. Column 6: the availability of data from the *Kepler* mission for this object (KO). "Y" means that the object has been observed by the *Kepler* mission, and hence that *Kepler* data is available. "N" means no *Kepler* data is available.
7. Column 7: the position of the slit (Slit). "×1" means that the fiber slit uses the full slit width ($R = 1000$). In case of "×2/3" or "×1/2," the fiber slit is limited to 2/3 ($R \sim 1800$) or half ($R = 2000$) of the slit width, respectively.
8. Column 8: the most recent version number of the pipelines for which the results are available (Version).

Table 5
Database of the LAMOST Spectra Obtained for the LK-project: Additional Information About the Cross-identified *Kepler*
Targets Extracted from the KIC (Brown et al. 2011)

(1) File Name (9) $T_{\rm eff}$ (K)	(2) Target (10) log g (dex)	(3) R.A. (hh:mm:ss) (11) $[M/H]$ (dex)	(4) decl. (dd:mm:ss) (12) $E(B-V)$ (mag)	(5) Ang (arcmin) (13) pm (arcsec yr^{-1})	(6) Con (14) pmR.A. (arcsec yr^{-1})	(7) Kp (mag) (15) pmdecl. (arcsec yr^{-1})	(8) MagDiff (mag) (16) Notes
spec-55712-IF10M_sp01-001 6116	KIC02140382 4.614	19:03:39.559 −0.319	37:32:54.92 0.127	0.003 0.017	⋯ 0.015	14.734 0.007	0.216
spec-55712-IF10M_sp01-002 5675	KIC01995622 4.223	19:04:44.213 −0.748	37:28:56.78 0.108	0.0006 0.004	0.034(#4) 0.003	13.517 −0.003	0.003
spec-55712-IF10M_sp01-003 	KIC01994759 0.000	19:03:42.471 0.000	37:29:40.58 0.000	0.002 	⋯ 	16.212 	0.518
spec-55712-IF10M_sp01-004 5916	KIC02141025 4.294	19:04:32.263 −0.096	37:33:38.95 0.151	0.001 0.010	0.066(#4) −0.003	14.827 −0.010	0.003
spec-55712-IF10M_sp01-005 6048	KIC01995904 4.281	19:05:02.777 −0.166	37:28:57.32 0.159	0.0007 0.000	0.116(#4) 0.000	14.944 0.000	−0.004
spec-55712-IF10M_sp01-006 6821	KIC02283124 4.232	19:04:08.376 0.045	37:39:53.24 0.114	0.001 0.011	0.023(#4) −0.002	12.622 −0.011	−0.002
spec-55712-IF10M_sp01-008 6067	KIC02283334 4.557	19:04:25.126 −0.170	37:36:15.12 0.151	0.0009 0.004	0.099(#4) 0.0002	15.372 −0.004	−0.002
spec-55712-IF10M_sp01-009 4910	KIC02282652 4.336	19:03:27.017 0.018	37:40:56.93 0.109	0.0007 0.005	0.068(#4) −0.005	15.005 0.0003	0.005
spec-55712-IF10M_sp01-010 5397	KIC02283496 4.438	19:04:37.339 −0.170	37:40:01.20 0.133	0.0001 0.010	0.118(#4) 0.009	15.286 −0.005	0.004
spec-55712-IF10M_sp01-011 5185	KIC02422998 4.644	19:04:46.178 −0.728	37:44:24.32 0.019	0.0005 0.0005	0.006(#4) −0.0001	10.630 −0.0003	0.000

Note. Only the first 10 entries are shown. For a description of the columns, we refer the reader to the text (see Section 7.2). For clarity, columns (9)–(16) are given on a second line for each entry.

(This table is available in its entirety in machine-readable form.)
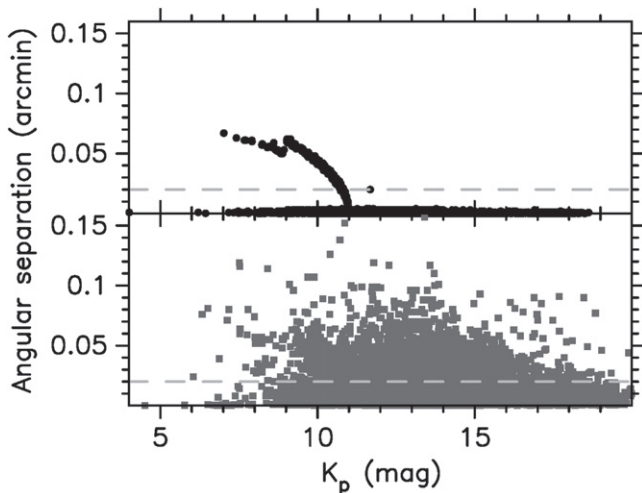
Figure 3. Overview of the angular separation (in arcmin) between the equatorial coordinates of the fibers as given in the headers of the LAMOST 1D fits files and the equatorial coordinates of the KIC objects they were cross-identified with (column 5 of Table 5) as a function of their *Kepler* magnitude Kp (column 7 of Table 5). The observed objects that were listed as a KIC object in the target list are given in the top panel (black dots). Those objects that were originally observed as field targets are given in the bottom panel (gray squares). The horizontal dashed lines in light gray indicate the standard search radius of 0.02 arcmin around the equatorial coordinates of the fibers during the cross-identification process.

The first two numbers refer to the reduction pipeline and the last number to the analysis pipeline.

9. Column 9: the R.A. of the fiber in degrees (R.A.deg). In general, it corresponds to the R.A. of the object as given in the target list (epoch 2000.0), except for a fraction of the targets brighter than magnitude 11, for which an offset is added to the pointings of the fibers to avoid saturation.
10. Column 10: same as column 9, but for the declination of the fiber in degrees (decl.deg).
11. Column 11: the type of magnitude as given in headers of the LAMOST 1D fits file (MAGtype).
12. Column 12: the brightness of the target in magnitude as given in headers of the LAMOST 1D fits file (MAG). Targets for which the brightness is not known have no entry in this column.
13. Column 13: the S/N in the r band (S/N$_r$). The entry "+99.99" means that S/N$_r$ > 100 but that the exact value is not given.
14. Column 14: note on the cross-identification as described above in the text (Notes).

For those targets identified with an object from the KIC, extra information extracted from the KIC is given in Table 5. There are 17,241 observed targets for which there are no KIC parameters available. Apart from the first two columns, which
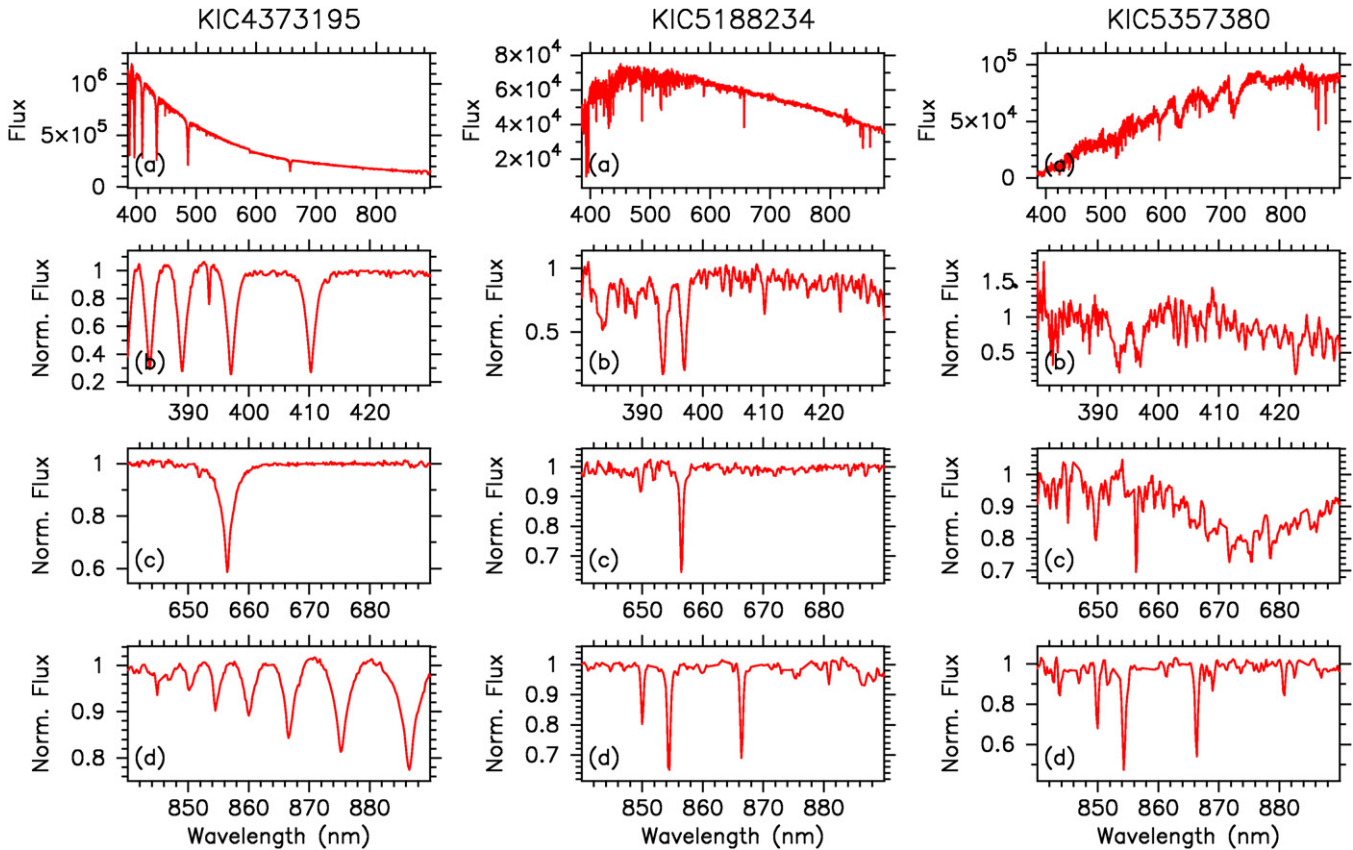
Figure 4. Examples of high-quality LAMOST spectra of KIC 4373195 (left), KIC 5188234 (middle), and KIC 5357380 (right) obtained during the LK-project. For each of these objects, we plot the approximately flux-calibrated spectra in the full observed wavelength range (panels (a)) and the continuum-normalized fluxes in three different wavelength regions: 380–430 nm (panels (b)), 640–690 nm (panels (c)), and 840–890 nm (panels (d)). The heliocentric radial velocity corrections were applied during the pipeline reductions. The sampling resolution in pixels varies with wavelength and averages 2.5 sampling pixels per resolution element (Luo et al. 2015).

are identical to those given in Table 4, Table 5 contains the following extra columns.

1. Column 3: the KIC right ascension in hh:mm:ss.sss (R.A.).
2. Column 4: the KIC declination in dd:mm:ss.ss (decl.).
3. Column 5: the angular separation in arcminutes between the equatorial coordinates of the fiber (columns 9 and 10 of Table 4) and the equatorial coordinates of the KIC object it was cross-identified with (columns 3 and 4 of this table; Ang)
4. Column 6: the contamination factor of those objects for which *Kepler* photometry is available (Con). The *Kepler* light contamination can be found for different seasons (season 0, 1, 2, and/or 3) with the *Kepler* Target search tool[30], where it is defined as the fraction of light in the aperture that is not due to the target star. We list the average value of the available seasons. The number of seasons used is given between brackets (see the discussion in Section 7.4.4).
5. Column 7: the *Kepler* Kp magnitude in mag (Kp).
6. Column 8: the difference between the magnitude as given in headers of the LAMOST 1D fits file (column 12 of Table 4) and the *Kepler* Kp magnitude of the KIC object it was cross-identified with (column 5 of this table; MagDiff).
7. Column 9: the KIC effective temperature in K ($T_{\rm eff}$).

8. Column 10: the KIC surface gravity in dex ($\log g$).
9. Column 11: the KIC metallicity in dex ($[M/H]$).
10. Column 12: the KIC reddening in mag ($E(B-V)$).
11. Column 13: the total proper motion in arcsec yr^{-1} (pm).
12. Column 14: the angular changes per year in right ascension in arcsec yr^{-1} (pmR.A.).
13. Column 15: the angular changes per year in declination in arcsec yr^{-1} (pmdecl.).
14. Column 16: note on the cross-identification as described above in the text (Notes).

These parameters are not available for every target in the KIC.

Tables 4 and 5 serve as input catalogs for the comparison of the results obtained in the other papers of this series.

7.3. Examples

As an example of the output of the LAMOST reduction pipeline, in Figure 4, we show the spectra of three stars with a very different SpT. The spectra are those of KIC 3756031 (left panels), KIC 8235498 (middle panels), and KIC 5357380 (right panels) classified by the 1D pipeline as A0-, G0-, and M1-type stars, respectively. The top panels (Figure 4 (a)) show the full 1D "flux-calibrated" spectra, while the lower panels display three portions of those spectra automatically normalized to the local continuum or pseudo-continuum. The most relevant lines, such as the high members of the Balmer series for the hot stars or the Ca II H & K lines for the cool ones, are evident in panels

---

[30] Parameters for *Kepler* targets can be found with the *Kepler* Target search tool: http://archive.stsci.edu/kepler/kepler_fov/search.php

(b) of Figure 4. The other two spectral segments contain Hα and the near-IR region (panels (c) and (d) of Figure 4, respectively). For hot stars, the near-IR region clearly shows several Paschen lines while the Ca II infrared triplet lines are visible for cool stars. All of these spectral features are fundamental for classification purposes.

There are three teams characterizing all of the observed targets by analyzing all of the available LAMOST spectra with sufficient quality. They all use a different approach and so the results of the different teams are independent.

The "Asian team" (A. B. Ren et al. 2015, in preparation) is performing a statistical analysis of the stellar parameters resulting from the LAMOST stellar parameter pipeline (LASP; Luo et al. 2015). It determines the stellar parameters ($T_{\rm eff}$, log g, [Fe/H]), $v_{\rm rad}$, and the spectral subclass. For the initial guess of the stellar parameters, the Correlation Function Interpolation method is used (Du et al. 2012). It searches for the best fit in a grid of 8903 synthetic spectra that was built by using the Kurucz spectrum synthesis code based on the ATLAS9 stellar atmosphere models provided by Castelli & Kurucz (2003). The final values are determined with a version of the Université de Lyon Spectroscopic analysis Software (Koleva et al. 2009) adapted to the LAMOST data. This is done by minimizing the squared difference between the observations and models. For the construction of the model corresponding to a set of values of the stellar parameters, an interpolator is used that runs over the whole ELODIE library (Prugniel & Soubiran 2001, 2004; Prugniel et al. 2007). For more details about the methods of the Asian team, we refer interested readers to Wu et al. (2011a, 2011b).

The "European team" (A. Frasca et al. 2015, in preparation) is determining the stellar parameters and the spectral classification with an adapted version of the code ROTFIT (Frasca et al. 2003, 2006). The observed spectra are fit to those available in a grid of spectra for a selection of more than 1000 comparison stars with known stellar parameters from the Indo-U.S. Library of Coudé Feed Stellar Spectra (Valdes et al. 2004). Because these spectra have a higher spectral resolution compared to LAMOST, they had to be degraded to match the low-resolution LAMOST spectra. As the library spectra are in the laboratory rest frame and are corrected for their heliocentric $v_{\rm rad}$, they also serve as templates to derive $v_{\rm rad}$ using the cross-correlation technique. Moreover, the analysis method is also capable of providing a rough estimate of $v \sin i$ for rapidly rotating stars.

The "American team" (R. A. Gray et al. 2015, in preparation) has developed the code MKCLASS for automatically classifying stars on the MK spectral classification system independent of the stellar parameter determination (Gray & Corbally 2014). This method requires a library of spectral standards and is designed to classify stellar spectra by direct comparison with MK standards using the same criteria as human classifiers. MKCLASS is capable of recognizing many of the common spectral peculiarities, including barium stars and carbon-rich giants, Ap and Am stars, λ Bootis stars, helium-weak and helium-strong B-type stars, etc. For the LAMOST classifications, the flux-calibrated standards library with 0.36 nm-resolution spectra obtained using the GM spectrograph at the Dark Sky Observatory of Appalachian State University is employed. Therefore, the LAMOST spectral resolution is slightly degraded to match that of the spectral library. The accuracy of the resulting classifications does not depend on the accuracy of the flux calibration of the LAMOST spectra. Based on tests of spectra classified by humans, the systematic error and standard deviation of the spectral and luminosity classes are 0.1 and 0.5 spectral sub-classes (where a unit spectral subclass is the difference between, for instance, F5 and F6) and 0.02 and 0.5 luminosity classes (where a unit luminosity class is the difference between, for instance, a dwarf (V) and sub-giant (IV) classification), respectively. Thus, the accuracy of MKCLASS is similar to the level of agreement obtained by two independently working skilled human classifiers.

In this paper, the results obtained by the different teams for a few example files are given only to illustrate their compatibility. Table 6 lists the stellar parameters as determined with LASP, ROTFIT, and MKCLASS for a variety of SpTs (late B/early A, late A/early F, late F/early G, late G/early K, and late K/early M). For each of these SpTs, we show the results for a spectrum with S/N$_r$ of >100, ~50, and ~20 from top to bottom. In general, the results for the stellar parameters $T_{\rm eff}$, log g, and [Fe/H] are fully compatible with each other. The few that do not agree within the formal errors are given in italics. They are found both among high and low S/N$_r$ LAMOST spectra. The agreement in the results for the spectral classification is less obvious. In those cases where the spectral sub-classes show a range of more than two, the results are given in italics. These differences are partly due to the bad coverage of certain SpTs in the grids of template spectra that were used for the LASP and ROTFIT calculations. For this reason, the results of MKCLASS should be considered as the most trustworthy. However, given the discrepancies in the standard templates, the agreement in SpTs, especially between ROTFIT and MKCLASS, is rather good, even for the lowest S/N$_r$.

In Figure 5, we show a statistical comparison of the stellar parameters obtained by the Asian team (LASP) and the European team (ROTFIT) based on the LAMOST spectra observed in 2011. The results for $T_{\rm eff}$, log g, and [Fe/H] derived from the 1035 LAMOST spectra that have been analyzed by both groups are given in panels (a)–(c), respectively. The overall agreement of the results is very good as the mean value and the standard deviation of the residuals amounts to -34 K and 221 K for $T_{\rm eff}$, -0.016 dex and 0.35 dex for log g, and -0.019 dex and 0.26 dex for [Fe/H], respectively. The intensity of the colors that are used are linked to the S/N$_r$ of the LAMOST spectrum that is analyzed: black corresponds to S/N$_r = 0$ while the lightest colors correspond to S/N$_r \geqslant 100$. Figure 5 shows that the results which deviate most significantly tend to originate from LAMOST spectra with a lower S/N$_r$ value. For $T_{\rm eff}$, the agreement of the results from both methods is excellent with no apparent systematic behavior, except for the hottest stars. This is likely due to the fact that the grids of the model spectra used in the analysis methods are sparse in this part of the Hertzsprung–Russel (H–R) diagram. For log g, the values provided by the two analysis codes agree quite well with each other, but the ROTFIT results appear to be clustered around 2.5 and 4.0 dex. This behavior may be due to the non-uniform density of the templates in the grid used by ROTFIT and in the ELODIE library used for interpolating in the LASP code. Indeed, these log g values are those typical for main-sequence and giant stars, respectively, which are much more frequent in these spectral libraries than stars with an intermediate log g or outside these ranges. For [Fe/H], the overall comparison is satisfactory but there seems to be a linear trend in the residuals that could be

Table 6
Representative Results Obtained by the Asian Team (LASP), the European Team (ROTFIT), and the American Team (MKCLASS)

File Name/Object	Version	S/N$_r$	SpT	T_{eff} (K)	log g (dex)	[Fe/H] (dex)	Method
spec-56094-kepler05B56094_2_sp13-034	v2.6.4	581	A2 V	9380(56)	3.5(11)	−0.35(5)	LASP
KIC 4373195	v2.4.3		B9 IV	9707(589)	3.83(11)	−0.16(14)	ROTFIT
*	v2.7.5		A0 IV–V				MKCLASS
spec-56096-kepler08B56096_1_sp07-250	v2.6.4	66	A2 V	11,223(113)	3.79(18)	−0.18(8)	LASP
KIC 3137033	v2.4.3		B9 III	10,839(342)	4.00(11)	−0.08(13)	ROTFIT
	v2.7.5		B9 V				MKCLASS
spec-56096-kepler08B56096_2_sp05-225	v2.6.4	23	A1 V	*10,869(241)*	3.87(25)	−0.41(15)	LASP
KIC 3654218	v2.4.3		B9 IV	*10,336(248)*	3.88(10)	−0.26(13)	ROTFIT
	v2.7.5		A1 IV				MKCLASS
spec-56096-kepler08B56096_1_sp02-050	v2.6.4	122	A9 V	*7,168(13)*	4.16(2)	*−0.42(3)*	LASP
KIC 3446837	v2.4.3		F0 V	*6,989(95)*	4.08(11)	*−0.13(13)*	ROTFIT
	v2.7.5		F2 IV–V Fe-0.6				MKCLASS
spec-56094-kepler05B56094_sp16-201	v2.6.4	65	F5	6593(30)	4.14(5)	−0.18(6)	LASP
KIC 5609930	v2.4.3		F0 V	6592(215)	4.10(13)	−0.16(15)	ROTFIT
	v2.7.5		F5 V				MKCLASS
spec-56094-kepler05B56094_sp12-098	v2.6.4	25	F5	6733(36)	4.10(6)	−0.22(7)	LASP
KIC 5449646	v2.4.3		F0 V	6820(281)	4.12(11)	−0.14(14)	ROTFIT
	v2.7.5		F3 V				MKCLASS
spec-56094-kepler05B56094_2_sp09-061	v2.6.4	279	G0	*5619(12)*	*3.63(4)*	−0.15(3)	LASP
KIC 5188234	v2.4.3		G0 V	*5774(97)*	*4.13(13)*	−0.11(17)	ROTFIT
*	v2.7.5		G0 IV–V				MKCLASS
spec-56094-kepler05F56094_sp15-020	v2.6.4	50	G0	5741(41)	4.30(12)	−0.33(10)	LASP
KIC 5095915	v2.4.3		G0 V	5731(91)	4.22(14)	−0.41(16)	ROTFIT
	v2.7.5		G1 V				MKCLASS
spec-56096-kepler08B56096_1_sp05-091	v2.6.4	17	F9	5765(76)	3.88(26)	−0.18(16)	LASP
KIC 3655915	v2.4.3		G0 V	5647(216)	4.05(25)	−0.43(20)	ROTFIT
	v2.7.5		G2 III–IV				MKCLASS
spec-56094-kepler05B56094_sp07-059	v2.6.4	114	G5	5325(15)	4.65(4)	−0.00(2)	LASP
KIC 2308241	v2.4.3		K0 V	5286(141)	4.54(15)	0.02(18)	ROTFIT
	v2.7.5		K2 V				MKCLASS
spec-56094-kepler05B56094_2_sp15-172	v2.6.4	46	K1	5336(28)	4.80(8)	0.17(5)	LASP
KIC 5442808	v2.4.3		K0 V	5162(157)	4.57(15)	0.05(12)	ROTFIT
	v2.7.5		K0 V				MKCLASS
spec-56094-kepler05F56094_sp13-172	v2.6.4	24	G5	*5285(66)*	*4.41(16)*	0.21(10)	LASP
KIC 4839014	v2.4.3		K0 V	*4968(191)*	*3.52(40)*	0.03(14)	ROTFIT
	v2.7.5		K0 V				MKCLASS
spec-56094-kepler05B56094_2_sp15-166	v2.6.4	219	M1	3717(7)	1.49(9)	−0.05(10)	LASP
KIC 5357380	v2.4.3		M1 III	3744(85)	1.47(15)	−0.07(13)	ROTFIT
*	v2.7.5		M0.5 II–III				MKCLASS
spec-56096-kepler08B56096_2_sp15-026	v2.6.4	44	M1	3754(21)	1.45(25)	−0.31(28)	LASP
KIC 6292615	v2.4.3		M1 III	3787(96)	1.52(17)	−0.09(13)	ROTFIT
	v2.7.5		M0.5 II				MKCLASS
spec-56096-kepler08B56096_2_sp13-010	v2.6.4	21	M0	3738(18)	1.31(19)	0.04(22)	LASP
KIC 5725850	v2.4.3		M1 III	3761(80)	1.50(15)	−0.05(11)	ROTFIT
	v2.7.5		M2 III				MKCLASS

Note. The results derived from the LAMOST spectra for examples of late B-/early A-, late A-/early F-, late F-/early G-, late G-/early K-, and late K-/early M-type stars are given from top to bottom. For each type, we give an example of a LAMOST spectrum with S/N$_r$ > 100, S/N$_r$ ~ 50, and S/N$_r$ ~ 20 (from top to bottom). For each spectrum, we give the name of the analyzed LAMOST spectrum and the KIC number of the observed target (File Name/Object; the LAMOST spectra indicated with ∗ are shown in Figure 4), the version of the pipelines that was used for each method (Version), the spectral classification (SpT), the effective temperature in K (T_{eff}), the surface gravity in dex (log g), the metallicity in dex ([Fe/H]), and the analysis method (Method; see Section 7.3 for more details about the methods used). The formal errors are given between brackets in units of the last decimal. The stellar parameters that do not agree within the formal errors and the spectral sub-classes with a range of more than two are given in italics.

due to similar contamination problems. Indeed, the metal-poor stars, as well as the very metal-rich ones, are far less frequent in these libraries.

Note that all of the LAMOST spectra shown in Table 6 were gathered during the pilot survey in 2012 June and that Figure 5

only shows results derived from the LAMOST spectra observed in 2011 during the test phase, and so the observation and pipeline procedures were not yet fully optimized. Hence, the discussion provided here can be considered as the worst case scenario. The full results obtained by the different teams will be given in the
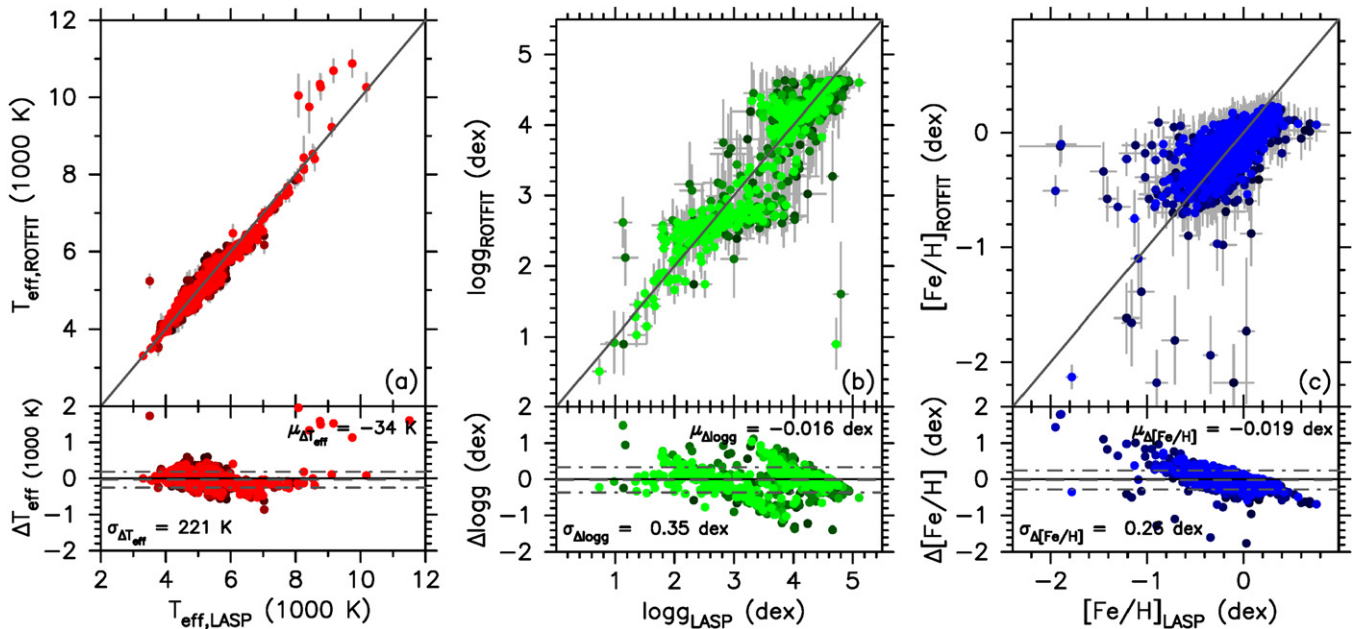
Figure 5. Statistical comparison of the stellar parameters obtained by the Asian team (LASP) and the European team (ROTFIT) from the LAMOST spectra observed in 2011. The results for T_{eff}, log g, and [Fe/H] are given in red, green, and blue in panels (a), (b), and (c), respectively. The intensity of the color is linked to the S/N$_r$ value of the LAMOST spectrum from which the results were derived, going from black for S/N$_r$ = 0 to light for S/N$_r \geqslant$ 100. In the top panels, we give the derived values as colored dots, the errors as light gray lines, and the bisector as a full dark gray line. In the bottom panels, we show the residuals as colored dots, the mean μ (given in the top right corner) as a dark gray dashed line, and the mean $\pm$ the standard deviation σ (given in the bottom left corner) as dark gray dashed–dotted lines.

following papers of this series. A more accurate and detailed statistical comparison of the results can only be done after the publication of the full results obtained by the different analysis teams.

7.4. Characterization

In this section, we discuss a few figures to characterize the database of the LK-project.

7.4.1. Objects

In Figure 6, we provide an overview of the objects in our database. The different types of targets are indicated with different colors. We use green for standard targets, blue for KASC targets, orange for planet targets, dark gray for extra targets, and light gray for field targets. The scientific importance of the different types of targets within the LK-project is also reflected in the size of the symbols. Note that only a few standard targets and field targets were observed, and so they are invisible on some of the panels in Figure 6.

The projection in equatorial coordinates is shown in Figure 6 (a). From this figure, it can be easily seen that the *Kepler* FOV is well covered by observations with LAMOST. Only a few parts are not covered: the center and off-center holes of the LK-fields (containing the central bright star and the guide stars, respectively; see Section 3), and the edge of one *Kepler* CCD (near R.A. ∼296° and decl. ∼51°). It also shows that there is overlap between the observed LK-fields.

Figure 6 (b) shows the magnitude distribution of the objects (column 12 of Table 4). The largest concentration of targets is found between magnitudes 12.5 and 14, which is a reflection of our observation strategy. Indeed, the observations only focused on very bright objects (Kp < 10.5) on two occasions (plates 110608_1 and 120604_1 in Table 3) and on faint objects on

four occasions (Kp > 14.0 for plates 120615_3 and 120617_3, and 140520_1, and Kp > 16.8 for plate 131002_1 in Table 3).

Figure 6 (c)–(e) give the distributions of the KIC stellar parameters of the observed objects: [M/H] (column 11 of Table 5), T_{eff} (column 6 of Table 5), and log g (column 10 of Table 5), respectively. The latter two distributions are visualized in a different way in Figure 6 (f) where the objects are placed in a Kiel diagram (log g versus T_{eff}), which is an alternative version of the H–R diagram. The distribution of the KIC [M/H] suggests that the majority of the objects are slightly metal-poor with a median value around −0.4 dex. A subset of 12,000 LAMOST spectra of stars from the LK-project have been used by Dong et al. (2014) to study the reliability of the metallicity values as given in the KIC catalog. They found that the true metallicity and the dynamic range of the *Kepler* sample are both systematically underestimated by the KIC. Hence, the KIC [M/H] values should be treated with caution. The majority of our objects have a KIC T_{eff} between 4000 and 7000 K. The *Kepler* field contains only a few hot stars for which the parameter determination based on Sloan photometry suffers most from the lack of an ultraviolet filter. The double-peak structure of the T_{eff} and log g distribution reflects the superposition of the main sequence (centered around T_{eff} ∼ 6000 K and log g ∼ 4.5 dex) and the red giant branch (centered around T_{eff} ∼ 4800 K and log g ∼ 2.7 dex).

There are no significant differences between the distributions of the different groups of targets, except for the spatial and brightness distributions: the standard targets are very bright, the KASC targets are mainly restricted to magnitude 12, while the other types of targets extend to fainter targets. Obviously, the gaps between the *Kepler* CCDs are filled by extra (dark gray dots) and field (light gray) targets (Figure 6(a)). The currently available LAMOST spectra of each type of target in itself (except the standard and field targets that are few) are appropriate to
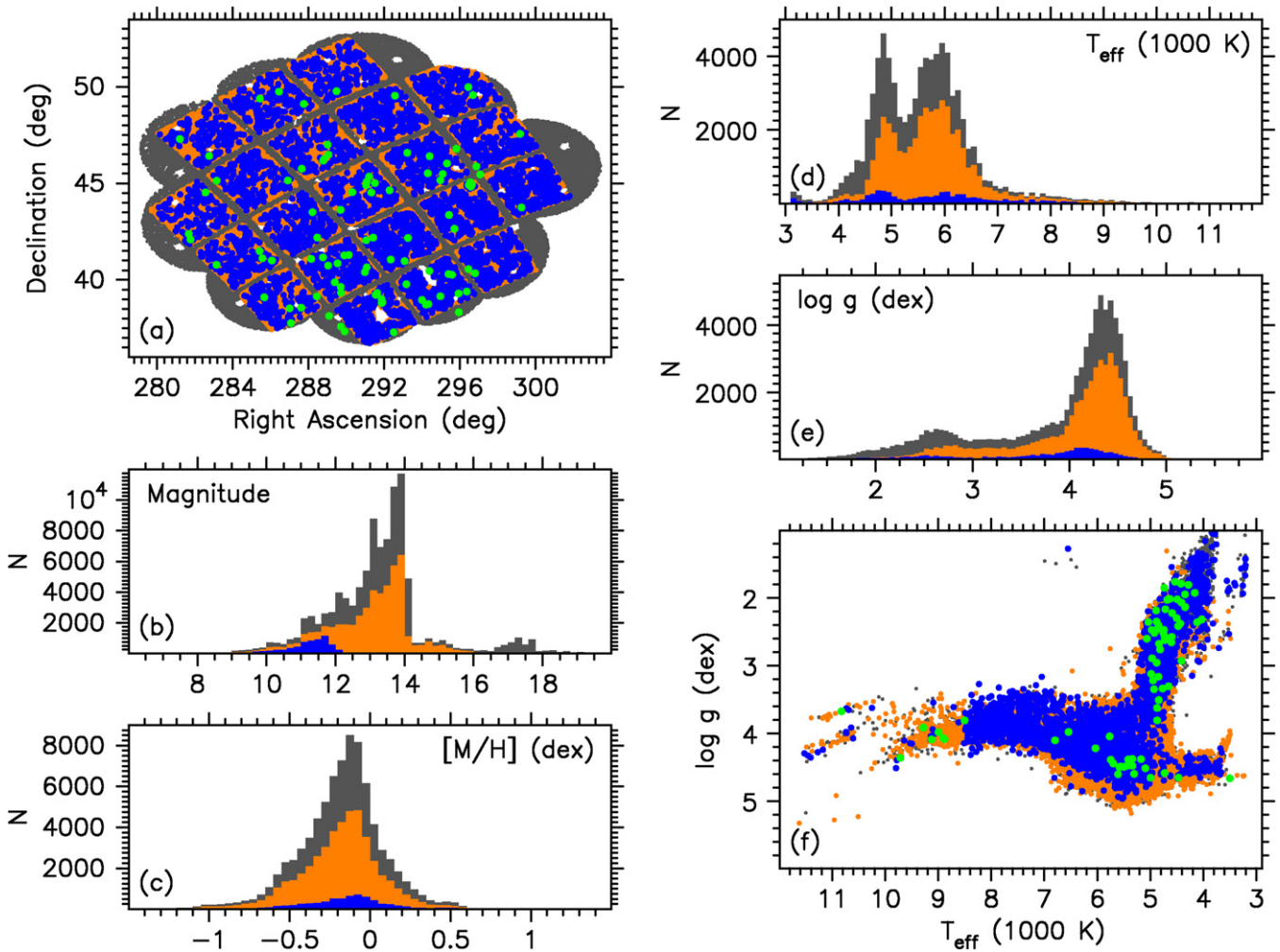
Figure 6. Global characterization of the objects in the database. The projection in equatorial coordinates (columns 9 and 10 of Table 4) of the available targets is shown in panel (a). We give the distribution of their magnitude (column 12 of Table 4; bin size of 0.2 mag), their KIC metallicity (column 11 of Table 5; bin size of 0.05 dex), their KIC effective temperature (column 9 of Table 5; bin size of 100 K), and their KIC surface gravity (column 10 of Table 5; bin size of 0.05 dex) in panels (b)–(e), respectively. The latter two distributions are represented in an alternative way by showing the position of the objects in a Kiel diagram (log g vs. T_{eff}). The following color coding is used (from high to low scientific importance; from bottom to top within the distributions): green for standard targets, blue for KASC targets, orange for planet targets, dark gray for extra targets, and light gray for field targets. The scientific importance of the different types of targets within the LK-project is also reflected in the size of the symbols in panels (a) and (f).

study their stellar parameters, thus tracing the target properties across the H–R diagram.

7.4.2. Multiple Observations

As there is considerable overlap between some of the observed LK-fields (Figures 2 and 6(a)), there are many objects that have been observed more than once: 14,186 objects have been observed two times, 2483 objects three times, 332 objects four times, and 113 objects at least five times (see the bottom rows of Table 1). Many of these objects are indeed found in the overlapping regions. Those within the non-overlapping regions are either objects that are observed on different plates of the same field or objects that are observed as a field star that turned out to be an already observed *Kepler* star (or vice versa). Even though the main aim of our LK-project is to determine the stellar parameters of as many objects within the *Kepler* FOV as possible, it is extremely valuable to have a significant number of objects with multiple LAMOST spectra as they can be used to check the consistency of the results of the analysis methods used and to discover stars with a variable v_{rad}. The distributions

of the parameters for the sub-sample of stars with multiple exposures are consistent with the general distributions shown in Figure 6. Hence, these targets can be used to check the consistency of the results across the H–R diagram.

7.4.3. Signal-to-noise Ratio

Figure 7 gives the distribution of the S/N in the *r* band (S/N_r) of the available LAMOST spectra (column 13 of Table 4). It gives an overview of the overall quality of the data. In this figure, we provide a histogram of the S/N_r values for two data sets: the full set of 101,086 LAMOST spectra that have been reduced (in gray) and the full data set restricted to the 42,209 LAMOST spectra with the highest S/N_r for the targets that have been observed by the *Kepler* mission (in black). The top and bottom panels give a global overview for S/N_r up to 200 and a detailed overview for the S/N_r range [0, 20], respectively. The small fraction of LAMOST spectra with $S/N_r \geqslant 200$ is not shown. We consider $S/N_r = 10$ as the strict minimum requirement for a LAMOST spectrum to be analyzed and $S/N_r = 20$ as the minimum requirement for an object to be
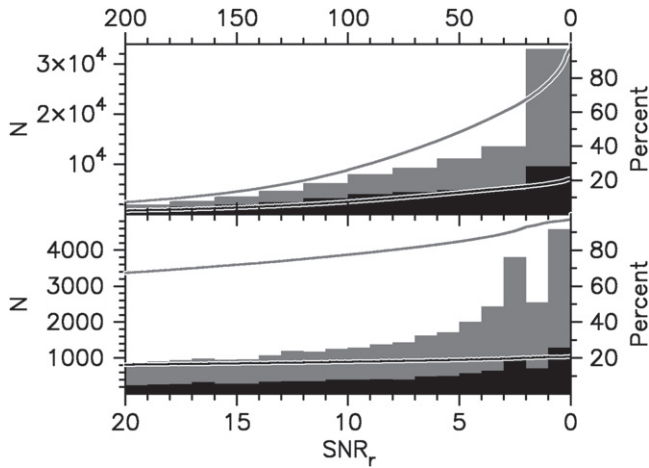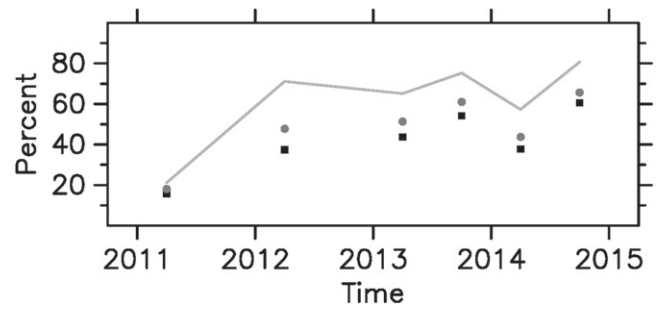
Figure 7. Histogram of the S/N values in the r band (S/N_r) of the LAMOST spectra (see column 13 of Table 4) for the regions [200, 0] (bin size 20; top) and [20,0] (bin size 1; bottom panel). The gray and black colors refer to the full data set (101,086 spectra) and to the full data set restricted to the spectrum with the highest S/N_r for the targets that have been observed by the *Kepler* mission (42,209 spectra), respectively. The full lines give the cumulative percentage of LAMOST spectra for each data set as a function of decreasing S/N_r value.

Figure 8. Overview of the evolution of the success rate of LAMOST during the LK-project over time. We show the percentage of the fibers leading to a successfully reduced LAMOST spectrum (light gray full line) and to a LAMOST spectrum with $S/N_r \geqslant 10$ (gray circle) and $S/N_r \geqslant 20$ (black square). The observations are subdivided into semesters: May–June and September–October of each year.

Figure 9. Overview of the *Kepler* contamination factors for objects in the database (column 6 of Table 5). A histogram with a bin size of 0.01 is given. The full lines give the cumulative percentage of targets as a function of increasing contamination factor.

removed from our target list for future observations. The full lines plotted on top of the histograms in each panel of Figure 7 give the cumulative percentage of LAMOST spectra for each data set as a function of decreasing S/N_r value. About 67.3% of the reduced LAMOST spectra have a $S/N_r \geqslant 20$ and about 77.5% have a $S/N_r \geqslant 10$. So far, we have LAMOST data for 21.1% of the 199,718 objects that have been observed during the *Kepler* mission, but not all of these LAMOST spectra are of a sufficient quality. For 17.9% of these *Kepler* mission targets, we have a LAMOST spectrum with a S/N_r above 10. For 16.3% of them, the S/N_r of their best LAMOST spectrum exceeds 20. These latter targets can be removed from the target list for future LAMOST observations.

The S/N_r can also be used to estimate the percentage of LAMOST fibers leading to high-quality data ($S/N_r \geqslant 20$) as a function of time. This is illustrated in Figure 8. During the test phase, high-quality LAMOST spectra emerged from about 15% of the fibers only while this percentage reached about 60% during the last semester. This is mainly due to an improvement in the fiber positioning and the better calibration of the LAMOST spectra. Also, the meteorological circumstances during the observations can have an effect on the overall quality of the LAMOST spectra. They can cause seasonal fluctuations but cannot be responsible for the clear upward trend seen in Figure 8.

7.4.4. Contamination

The *Kepler* contamination factor of an object tells us how much the *Kepler* light curves are affected by the presence of neighboring objects. The higher the *Kepler* contamination factor, the more overlap with neighboring objects, and hence the less reliable the results that can be derived from the *Kepler* data. As the LAMOST fiber size and typical seeing match the *Kepler* pixel size, the *Kepler* contamination factor can be used as an indication of how much the ground-based measurements of LAMOST can be expected to be affected by contamination effects. The *Kepler* contamination factor was not taken into account for the construction of the prioritized list of targets (see

Section 2). In Figure 9, we give the distribution of the *Kepler* contamination factor for the 50,053 observed objects for which a value can be found with the *Kepler* Target search tool. We used a bin size of 0.01 for the construction of the histogram. The full lines give the cumulative percentage of targets as a function of increasing contamination factor. The distribution peaks around a *Kepler* contamination factor of 0.025 and 89.77% of the objects have a value below 0.1, which means that the contamination effects for the vast majority of the objects are small. For 365 objects (0.73%), the *Kepler* contamination factor is higher than 0.5, which means that more than 50% of the counts in the light curves of these objects comes from neighboring objects. The LAMOST data for such objects should be interpreted with caution. We cannot rule out that in some cases that the wrong star was observed.

8. DISCUSSION

The LAMOST spectra described in the database of this paper have been proven to be of high scientific value, especially for the large community involved in the *Kepler* research. The LK-project has led to the first spectroscopic observation for many, generally relatively faint, *Kepler* targets. To maximize the visibility of the LAMOST spectra within this community, the observations are listed in the overview table with ground-based follow-up observations for *Kepler* targets on the web page of KASOC.[31]

The LAMOST spectra have already been used by several groups of astronomers. Apart from the three teams that are

---

[31] The KASOC web page (http://kasoc.phys.au.dk/) is a private web page that can be accessed by registered KASOC members only.

deriving stellar parameters from all of the good-quality LAMOST spectra, the data of the LK-project have been useful for selecting interesting targets for other types of studies. The wavelength coverage of the LAMOST observations includes the Lithium line at ~670 nm, making this survey ideal for identifying candidates with unusual Li abundances. Of particular interest are those KASC targets where oscillations have been detected, which allow us to place stringent constraints on the evolutionary phase and physical properties of the star. Thanks to our LAMOST survey, Silva Aguirre et al. (2014) have detected the first confirmed Li-rich core-helium-burning giant. The LAMOST observations also include the Ca II H & K lines at 396.85 and 393.37 nm, respectively (see Figure 4(b)), making it possible to measure the chromospheric activity of the observed stars. The most commonly used expression for stellar chromospheric activity is the dimensionless S index (Baliunas et al. 1995) and the excess flux (Hall et al. 2007). C. Karoff et al. (2015, in preparation) have measured both parameters for 7700 main-sequence solar-like stars with $T_{\rm eff}$ between 5000 and 6000 K in the *Kepler* field with LAMOST spectra using the same method that was used by Karoff et al. (2013). Bostancı et al. (2015) used the LAMOST spectra of members of NGC 6866 to derive the metallicity and the $v_{\rm rad}$ of this open cluster. Some individual LAMOST spectra from the LK-project have also been used in case studies: e.g., the red giant star KIC 5689820 (Deheuvels et al. 2014).

Even though the LAMOST spectra obtained during the test phase and the pilot survey for the LK-project have been proven to be of a sufficient quality for several scientific applications, the LAMOST observations and procedures are still being subjected to continuous improvements. For the general survey, the observation plan is better and resulted in a rapid increase in the data quantity, although more bright stars (<14 mag) are observed on bright nights. Also, the quality control has been improved, which makes the success rate of the observations reach 60%. As more of the acquired spectra reach a S/N_r level of 10, more data can be collected. There have already been several updates in the LAMOST reduction and analysis pipelines. For the faint objects, the sky subtraction now reaches the SDSS level while there are still some sky continuum problems for bright stars on bright moon nights. This issue can be solved by a better sky model. The difficulty of looking for standard stars in some spectrographs has been solved by using the estimates of the stellar parameters obtained before the flux calibration. Based on these parameter estimates, late F-type stars are selected as standard stars and the flux calibration for one spectrograph is performed by using the curve obtained by comparing the observed spectra with model spectra of standard stars. This makes it possible to connect almost all of the blue and red arm spectra and to improve the relative flux calibration. A more detailed description of the recent improvements and of the data process itself are given in Luo et al. (2015). Astronomers who need help processing LAMOST spectra they are interested in can contact the members of the LAMOST consortium.[32] The prospect for LAMOST is bright, and the observations for the LK-project will continue.

REFERENCES

Baliunas, S. L., Donahue, R. A., Soon, W. H., et al. 1995, ApJ, 438, 269
Batalha, N. M., Borucki, W. J., Koch, D. G., et al. 2010, ApJL, 713, L109
Bostanci, Z. F., Ak, T., Yontan, T., et al. 2015, MNRAS, 453, 1095
Brown, T. M., Latham, D. W., Everett, M. E., & Esquerdo, G. A. 2011, AJ, 142, 112
Bruntt, H., Basu, S., Smalley, B., et al. 2012, MNRAS, 423, 122
Bruntt, H., Frandsen, S., & Thygesen, A. O. 2011, A&A, 528, A121
Castelli, F., & Kurucz, R. L. 2003, in IAU Symp. 210, Modelling of Stellar Atmospheres, ed. N. Piskunov, W. W. Weiss & D. F. Gray (San Francisco, CA: ASP), 20P
Catanzaro, G., Frasca, A., Molenda-Żakowicz, J., & Marilli, E. 2010, A&A, 517, A3
Catanzaro, G., Ripepi, V., Bernabei, S., et al. 2011, MNRAS, 411, 1167
Cui, X.-Q., Zhao, Y.-H., Chu, Y.-Q., et al. 2012, RAA, 12, 1197
Cunha, M. S., Aerts, C., Christensen-Dalsgaard, J., et al. 2007, A&ARv, 14, 217
Deheuvels, S., Doğan, G., Goupil, M. J., et al. 2014, A&A, 564, A27
Dong, S., Zheng, Z., Zhu, Z., et al. 2014, ApJL, 789, L3
Du, B., Luo, A., Zhang, J., Wu, Y., & Wang, F. 2012, Proc. SPIE, 8451, 37
Frasca, A., Alcalá, J. M., Covino, E., et al. 2003, A&A, 405, 149
Frasca, A., Guillout, P., Marilli, E., et al. 2006, A&A, 454, 301
Gray, R. O., & Corbally, C. J. 2014, AJ, 147, 80
Hall, J. C., Henry, G. W., & Lockwood, G. W. 2007, AJ, 133, 2206
Karoff, C., Metcalfe, T. S., Chaplin, W. J., et al. 2013, MNRAS, 433, 3227

---

[32] Send requests to Dr. Ali Luo (lal@bao.ac.cn).

Koch, D. G., Borucki, W. J., Basri, G., et al. 2010, ApJL, 713, L79
Koleva, M., Prugniel, P., Bouchard, A., & Wu, Y. 2009, A&A, 501, 1269
Lehmann, H., Tkachenko, A., Semaan, T., et al. 2011, A&A, 526, A124
Luo, A.-L., Zhang, H.-T., Zhao, Y.-H., et al. 2012, RAA, 12, 1243
Luo, A.-L., Zhao, Y.-H., Zhao, G., et al. 2015, RAA, 15, 1095
McNamara, B. J., Jackiewicz, J., & McKeever, J. 2012, AJ, 143, 101
Michel, E. 2006, CoAst, 147, 40
Molenda-Żakowicz, J., Bruntt, H., Sousa, S., et al. 2010a, AN, 331, 981
Molenda-Żakowicz, J., Jerzykiewicz, M., Frasca, A., et al. 2010b, arXiv:1005.0985
Molenda-Żakowicz, J., Latham, D. W., Catanzaro, G., Frasca, A., & Quinn, S. N. 2011, MNRAS, 412, 1210
Molenda-Żakowicz, J., Sousa, S. G., Frasca, A., et al. 2013, MNRAS, 434, 1422
Monet, D. G., Levine, S. E., Canzian, B., et al. 2003, AJ, 125, 984
Niemczura, E., Murphy, S. J., Smalley, B., et al. 2015, MNRAS, 450, 2764
Prugniel, P., & Soubiran, C. 2001, A&A, 369, 1048
Prugniel, P., & Soubiran, C. 2004, arXiv:astro-ph/0409214
Prugniel, P., Soubiran, C., Koleva, M., & Le Borgne, D. 2007, arXiv:astro-ph/0703658

Silva Aguirre, V., Ruchti, G. R., Hekker, S., et al. 2014, ApJL, 784, L16
Su, D. Q., Cui, X., Wang, Y., & Yao, Z. 1998, Proc. SPIE, 3352, 76
Thygesen, A. O., Frandsen, S., Bruntt, H., et al. 2012, A&A, 543, A160
Tkachenko, A., Lehmann, H., Smalley, B., Debosscher, J., & Aerts, C. 2012, MNRAS, 422, 2960
Tkachenko, A., Lehmann, H., Smalley, B., & Uytterhoeven, K. 2013, MNRAS, 431, 3685
Uytterhoeven, K., Briquet, M., Bruntt, H., et al. 2010a, AN, 331, 993
Uytterhoeven, K., Szabo, R., Southworth, J., et al. 2010b, arXiv:1003.6089
Valdes, F., Gupta, R., Rose, J. A., Singh, H. P., & Bell, D. J. 2004, ApJS, 152, 251
Wang, S.-G., Su, D.-Q., Chu, Y.-Q., Cui, X., & Wang, Y.-N. 1996, ApOpt, 35, 5155
Wu, Y., Luo, A.-L., Li, H.-N., et al. 2011a, RAA, 11, 924
Wu, Y., Singh, H. P., Prugniel, P., Gupta, R., & Koleva, M. 2011b, A&A, 525, A71
Xing, X., Zhai, C., Du, H., et al. 1998, Proc. SPIE, 3352, 839
Zhao, G., Zhao, Y.-H., Chu, Y.-Q., Jing, Y.-P., & Deng, L.-C. 2012, RAA, 12, 723